energies
MDPI

Review

Focussed Review of Utilization of Graphene-Based Materials in Electron Transport Layer in Halide Perovskite Solar Cells: Materials-Based Issues

Xinchen Dai [1], Pramod Koshy [1], Charles Christopher Sorrell [1], Jongchul Lim [2,*] and Jae Sung Yun [3,*]

[1] School of Materials Science and Engineering, UNSW Sydney, Sydney 2052, Australia; Xinchen.dai@student.unsw.edu.au (X.D.); koshy@unsw.edu.au (P.K.); c.sorrell@unsw.edu.au (C.C.S.)
[2] Graduate School of Energy Science and Technology, Chungnam National University, Daejeon 34134, Korea
[3] Australian Centre for Advanced Photovoltaics (ACAP), School of Photovoltaic and Renewable Energy Engineering, UNSW Sydney, Sydney 2052, Australia
* Correspondence: jclim@cnu.ac.kr (J.L.); j.yun@unsw.edu.au (J.S.Y.)

Received: 21 October 2020; Accepted: 27 November 2020; Published: 1 December 2020

Abstract: The present work applies a focal point of materials-related issues to review the major case studies of electron transport layers (ETLs) of metal halide perovskite solar cells (PSCs) that contain graphene-based materials (GBMs), including graphene (GR), graphene oxide (GO), reduced graphene oxide (RGO), and graphene quantum dots (GQDs). The coverage includes the principal components of ETLs, which are compact and mesoporous TiO_2, SnO_2, ZnO and the fullerene derivative PCBM. Basic considerations of solar cell design are provided and the effects of the different ETL materials on the power conversion efficiency (PCE) have been surveyed. The strategy of adding GBMs is based on a range of phenomenological outcomes, including enhanced electron transport, enhanced current density-voltage (J-V) characteristics and parameters, potential for band gap (E_g) tuning, and enhanced device stability (chemical and environmental). These characteristics are made complicated by the variable effects of GBM size, amount, morphology, and distribution on the nanostructure, the resultant performance, and the associated effects on the potential for charge recombination. A further complication is the uncertain nature of the interfaces between the ETL and perovskite as well as between phases within the ETL.

Keywords: perovskite solar cells (PSCs); electron transport layer (ETL); graphene-based materials (GBMs)

1. Introduction

Rapidly increasing global demands for clean energy supplies have created an imperative for increased utilization of renewable energy sources. Solar power is one such resource that can play such a major role. However, as a potential next-generation power supply, photovoltaic technologies must meet the requirements of cost-efficiency as well as environmental stability. Single-crystal and polycrystalline silicon solar cells are the most mature commercial photovoltaic devices, having achieved high efficiencies of >22% and considerable stability [1]. There also are low-cost commercial thin-film solar cells that have been developed as substitute materials, including amorphous silicon (a-Si:H), with a peak efficiency of 14%, and cadmium telluride (CdTe), with a peak efficiency of 22% [2]. Other emerging alternative thin-film solar cells utilize organic materials as light harvesters, and these can contribute to the reduction of noble element consumption and minimize production costs.

Metal halide perovskite solar cells (PSCs) were reported in 2009 and, since then, have gained increasing attention owing to their excellent power conversion efficiencies (PCEs) and low-cost fabrication [2,3]. Perovskite materials have the formula ABX_3, where A and B are different cations and

X is an anion. However, the most widely investigated perovskite for solar cells is an organic-inorganic halide, where the A site is occupied by an organic molecule, such as methylammonium (MA) or formamidinium (FA); the B site is occupied by Pb; and the X site is one of three halogens (Cl, Br, or I). To date, there has been very substantial improvement in the PCEs of perovskite solar cells, from 3.8% in 2009 for a dye-sensitized cell to the recently certified record for a perovskite cell of 25.5% in 2020 [4,5]. Other recent work has shown that metal halide perovskites exhibit superior optoelectronic properties, including high absorption coefficient [6,7], tunable band gap [8,9], long carrier diffusion length [10,11], good defect-tolerance [12], and high ambipolar charge carrier mobility [13]. These attributes have been enhanced through the fabrication of mixed perovskites, consisting principally of mixed A-site cations, mixed X-site halide anions, and simultaneously mixed A-site and X-site ions. These modifications have reported the effects of what is assumed to be substitutional solid solubility on band gap tuning, charge carrier transport, phase stability, and PSC stability [14].

In addition to the engineering of the perovskite materials themselves, considerable research has been done on the enhancement of the properties of the electron transfer layer (ETL). The ETL is a key component in PSCs because it enhances the extraction and transfer of electrons and acts as an interface to prevent charge recombination [15,16]. Conventional inorganic materials, such as TiO_2, SnO_2, and ZnO, have been used as ETLs in n-i-p (n-type–intrinsic–p-type, conventional) structure PSCs. Organic materials, such as fullerene and fullerene-derivatives (e.g., phenyl-C_{61}-butyric acid methyl ester (PCBM)), have been used widely as ETLs in p-i-n (p-type–intrinsic–n-type, inverted) structure PSCs. These designs incorporate a hole transfer material (HTM), which lead to the general designs of these PSCs as ETL–perovskite–HTM (n-i-p) and HTM–perovskite–ETL (p-i-n) structure. As these phases are deposited sequentially, with the ETLs being deposited first, and then heat treated, the ETL characteristics also can affect the wetting, recrystallization, and nanostructural development of perovskites through surface energy effects [17–22]. The characteristics that define a high-quality ETL are high electrical conductivity, high electron mobility, rapid electron extraction and transfer, wide band gap, close conduction band minimum (CBM) energy levels (lower than that of the perovskite and higher than that of the anode), wettability by the perovskite precursor, and uniform nanostructure (flat, dense, and homogeneous) [23–27].

In order to enhance the performance of the ETL, chemical modification by doping, microstructural modification by lamination or composite fabrication with a second semiconductor, and ETL surface passivation have been examined. For example, Mg-doping of a TiO_2 ETL improved the CBM alignment with that of the perovskite [28]. Mg-doping of a SnO_2 ETL reduced cracking, thereby increasing the uniformity and flatness of the ETL and improving interfacial contact with the perovskite layer [29]. These alterations resulted in improved electron transport within the devices. The use of a laminated ETL, such as TiO_2/SnO_2 was reported to enhance the long-term stability of PSCs and improve the perovskite stability under UV illumination [30]. An ETL with a core-shell MgO/TiO_2 composite microstructure reduced the rate of interfacial charge recombination [31]. Other studies have shown that surface passivation by the deposition of a thin layer of lithium bis(trifluoromethylsulphonyl)imide (Li-TFSI) on the top surface of the ETL passivates the electron traps and hence enhances the semiconducting properties [32,33]. The deposition of PCBM on the ETL surface has been reported widely to passivate the surface defects within the metal oxide ETL, thus enhancing electron transfer [34–37]; this reduced the hysteresis in PSCs [38].

The configuration of an ETL containing a graphene-based material (GBM) as a second phase recently has attracted attention. The principal advantages of using a GBM as a passivating or sandwich surface layer on the ETL or as a second-phase addition to the ETL are its capacity to improve the intrinsic semiconducting properties of the ETL and to alter the surface and volume morphologies of the ETL beneficially [17,39]. The effectiveness of GBMs can be increased through functionalization of GBMs with organic or inorganic molecules and through chemical surface modification [40]. Through these strategies, the semiconducting properties and surface chemistry can be tuned for adaptability to different ETLs and corresponding PSCs.

Although PCBM is used commonly as a passivating layer on the ETL, its organic nature limits its stability such that it can be damaged or removed relatively easily with the nonpolar solvents that are used in the commonly applied sol-gel processing of PSCs [41,42]. In contrast, GBMs as passivating and sandwich layers exhibit excellent mechanical properties and considerable chemical stabilities, thereby enhancing the stability of PSCs [43]. As composite additions, GBMs can be incorporated relatively easily into different types of conventional ETL materials, including TiO_2, SnO_2, ZnO, and PCBM, again offering mechanical advantages with little risk of chemical reaction.

The present work briefly reviews the utilization of GBMs in the ETLs of PSCs and their impact on the PCE. The effects of the use of GBMs in the ETLs on the nanostructural characteristics of the ETL and the alteration of the perovskite layer by the ETL also are considered. The most commonly used GBM-modified ETLs used in PSCs, which are TiO_2, SnO_2, ZnO, and PCBM, are discussed. A better understanding of these effects may facilitate enhancements in the performance of PSCs through improvements in the PCEs.

2. GBMs

In order to enhance the optoelectronic properties of PSCs, graphene-based derivatives have been investigated and utilized extensively [44,45]. Graphene (GR) is a 2D material with a single layer of sp^2-bonded carbon atoms that are tightly connected in a hexagonal honeycomb lattice. It exhibits remarkable electrical, optical, and mechanical properties as well as good stability, making it a good candidate to enhance the performance of PSCs [46]. Despite these excellent properties, pure GR exhibits zero band gap (E_g), which precludes its use as a semiconductor. However, chemical synthesis rarely produces pure GR, so what often is reported as GR is slightly impure. Compared to graphene, graphene derivatives are E_g-tunable and relatively low-cost materials that involve less complex fabrication methods. The most commonly used graphene derivatives are, as shown in Figure 1a, graphene oxide (GO), reduced graphene oxide (RGO), and graphene quantum dots (GQDs) that contain hydroxyl and carboxyl functional groups [47–49], which enable them to display hydrophilicity instead of hydrophobicity that is seen in graphene. These functional groups are beneficial to dispersibility in suspensions during processing using water and organic media of high dielectric constants [50]. The flexibility of GBMs has allowed them to be used in different parts of PSCs, including electrodes [51,52], perovskite layer [53,54], charge-transfer layer [55–59], and as interfacial layer [60–62].

There have been extensive works on GBMs for the ETL [17–20,23–27,39,43,55,56,60,61,63–81] that is sandwiched between the transparent conducting oxide (TCO) anodic substrate (layer 1) and the perovskite (layer 3), as shown in Figure 1b. ETL materials, such as TiO_2, SnO_2, ZnO, PCBM, $SrTiO_3$ + Al_2O_3, and Fe_2O_3, have been modified using GR, GO, RGO, and GQDs. The improvement in the PCE due to the modification by GBMs in ETLs is summarized in Figure 1c. There are eight reported GBM-modified ETLs in the green area of Figure 1c, which indicates the most effective ETL configurations using GBMs. Of the high-performance solar cells with PCEs $\geq$ 19%, Tavakoli et al. [43] and Mahmoudi et al. [55] reported a PCE > 30% with the use of a GBM sandwich layer. GQDs and GR have been shown to be the best GBM candidates, as exemplified by PCE improvements from 14.0% to 19.2% [77] and 13.82% to 19.81% [43]. In addition, PSCs with SnO_2 GQDs have yielded a PCE as high as 21.1% [19].

Figure 2 illustrates the energy levels of PSC component layers, including ETLs that have been modified using GBMs relative to the GBM-free analogues. As the ETL is required to extract and transport electrons as well as to block hole transport from the perovskite layer, materials suitable for ETLs should possess CBM or lowest unoccupied molecular orbital (LUMO) levels slightly lower than those of the perovskites; this situation enables electron transfer from the former to the latter. At the same time, ETLs should possess valence band maximum (VBM) or highest occupied molecular (HOMO) levels considerably lower than those of the perovskites; this situation prevents holes from entering the ETLs. The addition of GBMs can be used to tune the band energy levels of ETLs, viz., engineer the E_g, in order to achieve these ends in PSCs. For the entire cell, the direction of electron transport also requires the electrode (cathode) VBM to be above that of the HTM and that of the HTM to be above that of the perovskite as well as the CBM of the TCO (anode) to be below that of the ETL. Of course, this configuration also meets the requirement for the counter-transport of holes.

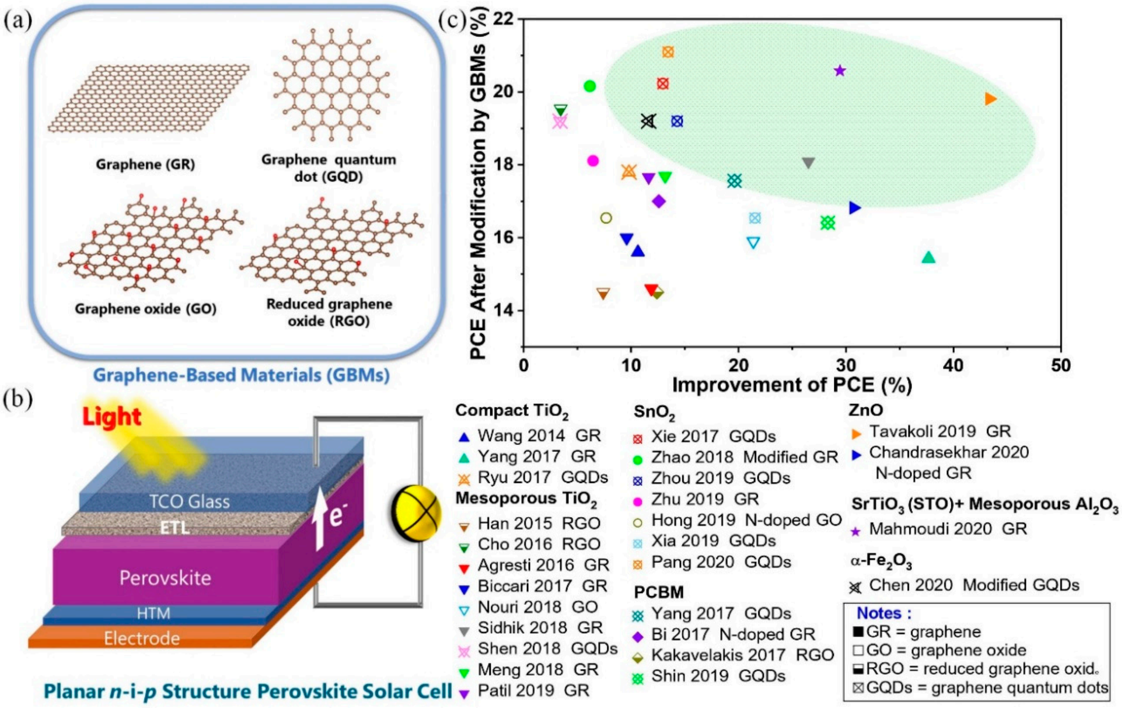

Figure 1. (**a**) Schematic of structures of graphene and its derivatives, (**b**) schematic cross section of planar n-i-p structure PSC, (**c**) comprehensive summary of power conversion efficiency (PCE) data for halide perovskite solar cells (PSCs) with electron transport layers (ETLs) comprised of graphene-based materials (GBMs) (power conversion efficiency (PCE) > 14%) [17–20,23,25–27,39,43,55,56,60,63–74] (TCO = transparent conducting oxide, HTM = hole transport material, green area = most efficient configurations for GBM-modified ETLs).

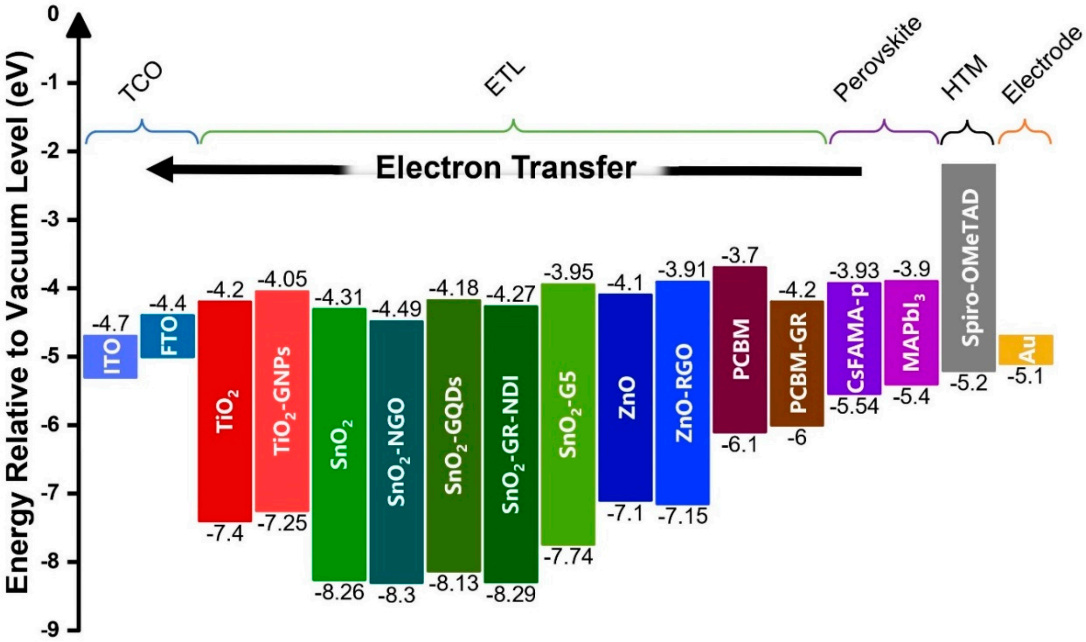

Figure 2. Reported CBM (conduction band minimum or lowest unoccupied molecular orbital, top) and VBM (valence band maximum or highest occupied molecular orbital, bottom) energy levels of TCO substrates, ETLs that have been modified using GBMs, HTM, and electrode [17,19,24,26,60,71,81]. ITO = indium tin oxide, FTO = fluorine-doped tin oxide, GNPs = graphene nanoplatelets, NGO = nitrogen-doped graphene oxide, NDI = napthalenetetracarboxylic diimide, G5 = 5 nm Ø GQDs, PCBM = fullerene derivative phenyl-C61-butyric acid methyl ester, NGR = N-doped graphene, CsFAMA-p = cesium containing mixed-cation mixed-halide perovskite, $MaPbI_3$ = methylammonium lead triiodide perovskite, Spiro-OMeTAD = 2,2′,7,7′-tetrakis(N,N-di-p-methoxyphenyl-amine)9,9′-spirobifluorene.

3. TiO_2

TiO_2 is the most widely used ETL material for n-i-p structure PSCs [5]. TiO_2 exists as two main polymorphs, anatase and rutile, where the latter is more thermodynamically stable [82]. Although the anatase → rutile phase transformation temperature is variable, the commonly cited temperature is ~600 °C. Two of the key influences on this temperature are impurities and dopants, so the composition of the adjacent perovskite layer is relevant because its cations tend to promote (A site cations of 2+ valence) or inhibit (B site cations of 4+ valence) this phase transformation. Both polymorphs have been reported to be present in PSCs [83–86]. Which polymorph is present is important because rutile has a lower E_g (~3.0 eV) than that of anatase (~3.2 eV) but the electron-hole recombination rate of the latter is slower [82].

TiO_2 can be presented in ETLs in two nanostructural forms, viz., compact (dense) TiO_2 (c-TiO_2) and mesoporous TiO_2 (m-TiO_2) [87]. In ETLs, TiO_2 is present as either a bilayer structure of compact plus mesoporous TiO_2 or a monolayer of compact TiO_2 alone. The c-TiO_2 layer acts as a hole blocker [28] while the m-TiO_2 offers the advantage that penetration of the perovskite liquid sol-gel precursor in the mesopores results in increased contact surface area and hence enhanced electron transfer [15]. The use of bilayer TiO_2 is a common and effective way to configure high-performance PSCs of high PCE, as reflected by reduced forward and reverse current-voltage (I-V) hysteresis [88,89]. High PCEs result from these nanostructural characteristics as well as the favorable TiO_2 E_g of ~3.0 eV or ~3.2 eV and CBM level of about -4.4 eV, which allow easy extraction and transfer of electrons from the perovskite layer and higher electron lifetimes. Additional advantages are relatively simple fabrication processes (e.g., spin coating of dispersions or sol-gel dispersions [15,28,83]) and low fabrication costs (e.g., ≤1 h at 100–500 °C sintering). However, TiO_2 has a low bulk electron mobility (1 cm^2/V s); TiO_2 polymorph not specified [90]) and TiO_2 may reduce the stability of the adjacent perovskite layer owing to the former's photocatalytic properties under UV illumination [91]. Consequently, the modification of TiO_2 to overcome these two shortcomings has been the subject of recent research.

3.1. Compact TiO_2 Layer

Wang et al. [63] were the first to report the use of a TiO_2-GR ETL layer in an n-i-p structure PSC. The addition of graphene to the c-TiO_2 layer of bilayer TiO_2 not only enabled the low-temperature fabrication at 150 °C but it also improved the PCE performance to a maximum of 15.6% from the 10.0% obtained from TiO_2 alone. The optimal amount of 0.6 wt % graphene addition contributed to an average open-circuit voltage (V_{oc}) of 1.05 V, a high short-circuit current density (J_{sc}) of 21.9 mA/cm^2, and a high fill factor (FF) of 0.73.

Ryu et al. [18] were the first to coat TiO_2 with GQDs (14, 10, or 7 nm size). The devices consisted of an TCO/ETL/perovskite/HTM/electrode configuration using the materials FTO/c-TiO_2/perovskite/Spiro-OMeTAD/Au for an n-i-p structure PSC. An average PCE of 17.80% was achieved using 14 nm GQDs, representing an ~8% improvement relative to the reference PSC average of 16.48%. O_2 plasma treatment was found to be beneficial to improved bonding between the TiO_2 and GQDs, as suggested in the corresponding FTIR spectra shown in Figure 3a. After O_2 plasma treatment, the appearance of two absorption bands at 1640 cm^{-1} and 1070 cm^{-1} is attributed to carboxylate bonding between the TiO_2 and GQDs. This carboxylate bonding would facilitate the electron transfer from the GQDs to the c-TiO_2.

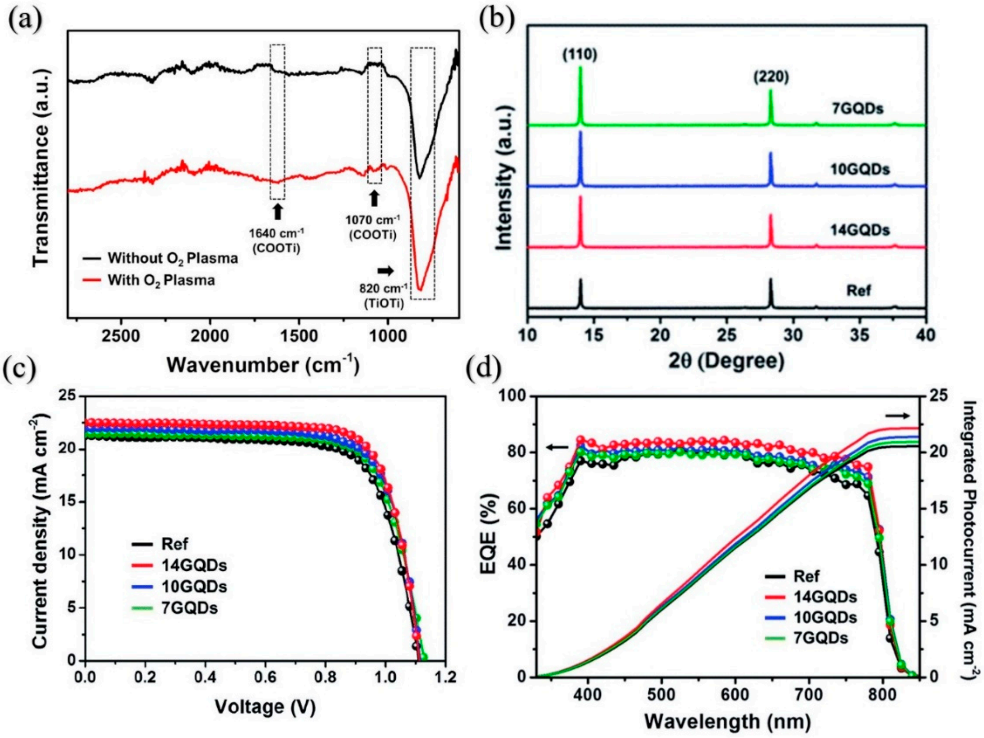

Figure 3. (**a**) FTIR spectra of TiO_2-GQDs with and without O_2 plasma treatment, (**b**) XRD patterns of perovskite on pristine TiO_2 and TiO_2-GQDs (14 nm, 10 nm, 7 nm), (**c**) current density-voltage (J-V) characteristics of PSCs, (**d**) external quantum efficiency (EQE) (or incident photon-to-current efficiency (IPCE)) spectra and integrated photocurrents of PSCs [18] (republished with permission from the Royal Society of Chemistry, conveyed through Copyright Clearance Center, Inc.).

The introduction of different sizes of the GQDs also contributed to improved recrystallization of the perovskite [18]. Figure 3b shows increased (110) perovskite X-ray diffraction (XRD) peak intensities of the TiO_2-GQD ETLs relative to the reference ETL. The effects of the GQDs on the electron transport properties also were analyzed and these revealed that the GQD CBM level could be tuned and lowered to closer proximity to the TiO_2 CBM level, which had a significant impact on control of the charge transfer behavior and efficiency. Further, the lower CBM level was effective in electron extraction, as revealed by an increased quenching level in steady-state photoluminescence (PL) spectra. The resultant current density (J) increased proportionally with GQD size, as shown in Figure 3c, and the external quantum efficiency (EQE, which also is known as the incident photon-to-current efficiency, IPCE), as well as the integrated photocurrent measurements, as shown in Figure 3d.

3.2. Mesoporous TiO_2 Layer

The utilization of GR and GBMs to modify the semiconducting properties of m-TiO_2 also has been reported. Han et al. [23] reported an m-TiO_2-RGO nanocomposite as ETL in n-i-p structure PSCs with improved electron transfer properties. The m-TiO_2-RGO was fabricated by mixing a TiO_2-ethanol slurry in various TiO_2/RGO volume ratios and spin coating. The successful incorporation of RGO in m-TiO_2 was confirmed by micro-Raman microspectroscopy using the RGO peaks at 1350 cm^{-1} (D band) and 1580 cm^{-1} (G band). The optimal concentration of RGO was found to be 0.4 vol%, which resulted in a PCE and J_{sc} increases from 11.5% to 13.5% and 19.6 mA/cm^2 to 21.0 mA/cm^2, respectively.

The improved PCE after the addition of RGO was attributed to the resultant lower resistivity and reduced charge recombination [23]. Hall measurements showed that the resistivity of the composite with 0.4 vol% RGO decreased by an order of magnitude. Reduced series resistance and charge recombination were demonstrated by electrochemical impedance spectroscopy (EIS). Further, the work function (Φ) of the RGO of −4.4 eV was lower than and close to the CBM of perovskite (−3.93 eV), thus facilitating electron transfer from the perovskite to the RGO.

Sidhik et al. [17] modified m-TiO_2 by adding graphene nanoplatelets (GNPs) and spin coating the resultant dispersions. A PSC with 2 wt % GNP achieved a maximal PCE of 19.23% and a fill factor of 80% owing to the CBM band alignment and consequent efficient electron transport. The authors speculated that the GNPs passivated the surface defects of TiO_2 and so reduced charge recombination. This was examined through the XPS data shown in Figure 4a for the O_{1s} peak of TiO_2, which was deconvoluted into the $I_{Ti\text{-}O}$ peak for lattice oxygen at 530.32 eV and the I_o peak for an oxygen vacancy at 532.6 eV. Their varying ratios reveal that the lowest $I_O/I_{Ti\text{-}O}$ was for the 2 wt % GNP ETL. This maximum was supported by photoluminescence (PL) data, shown in Figure 4b, which also suggested that the addition of 3.0 wt % GNP resulted in the generation of an unspecified type of surface defect. It also is possible that the higher amount of GNPs resulted in agglomeration and consequently reduced surface coverage. A further potential benefit of the coverage by GNPs was a reduction in surface roughness owing to the filling of the troughs, which would have increased the extent of the effective m-TiO_2/perovskite surface apposition and consequent electron transport and PCE.

Cho et al. [65] fabricated mesoporous ETLs from spin coated mixtures of TiO_2 and RGO, sintered them, and then treated the surface with Li-TFSI in order to facilitate electron injection into the ETL. The PSCs exhibited a maximal PCE of 19.54%. The incorporation of RGO led to quenching in time-resolved PL, indicating efficient electron extraction by the ETL owing to a synergistic effect between the Li-TFSI and RGO. The PSC also exhibited enhanced V_{oc} and FF without impacting on the carrier-transfer rate. Biccari et al. [20] compared the characteristics of two configurations of ETLs in $MAPbI_3$ PSCs, both of which included a perovskite/m-TiO_2 interlayer of spin coated lithium-neutralized graphene oxide (GO-Li). The m-TiO_2 interlayers differed in that one consisted of spin coated m-TiO_2 and the other consisted of spin coated m-TiO_2-GR. These devices exhibited well crystallized perovskite identified as tetragonal at all temperatures. The PL spectra at the same excitation energy of the configuration with m-TiO_2-GR revealed an order of magnitude lower trap density. Additionally, the carrier collection efficiency of the configuration with m-TiO_2-GR approximately doubled. Agresti et al. [61] used an FTO/c-TiO_2/m-TiO_2-GR/GO-Li/perovskite/Spiro-OMeTAD/Au configuration for PSCs of 50.6 cm^2 area module which achieved enhanced performance and stability. The PCE increased from 11.6% for a PSC without GR or GO-Li to 12.6% with these materials.

The long-term performance was very good on the device with only m-TiO_2-GR, retaining ~91% of the initial PCE after 1630 h (in the dark, dry conditions (humidity rate < 30%) and at open circuit).

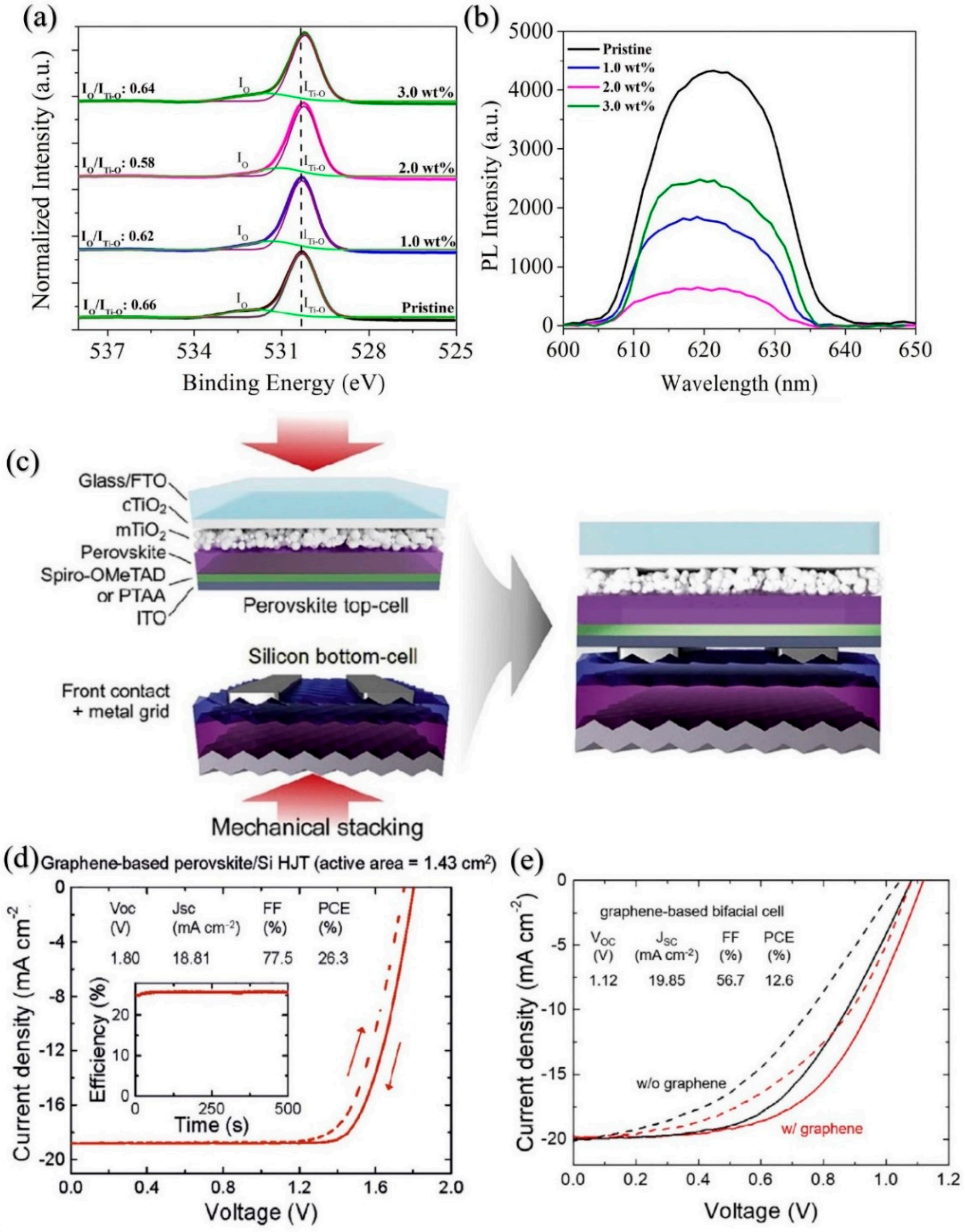

Figure 4. (**a**) O_{1s} XPS spectra for TiO_2 of different graphene nanoplatelets (GNP) additions, (**b**) photoluminescence (PL) spectra of TiO_2 of different GNP additions [17] (republished with permission from American Chemical Society), (**c**) schematic of cross section of two-terminal perovskite/silicon heterojunction (JHT) tandem solar cell by mechanical stacking of layers and uniaxial pressing, (**d**) J-V characteristics and parameters measured for tandem solar cell (inset shows stabilized (PCE)), (**e**) J-V characteristics and parameters measured for bifacial PSC with and without graphene (GR) in the TiO_2 bilayer ETL [79] (republished with permission from Elsevier).

Shen et al. [39] infiltrated m-TiO_2 with a GQD dispersion (1 mg/mL) by pre-sintering the m-TiO_2 layer, soaking in the GQD dispersion for 10 s, spin coating once or twice with the same dispersion, and heating at 100 °C for 30 min. Modification of the ETL of the PSC in this way enhanced electron extraction and so facilitated charge transport. Again, the deposition of GQDs smoothed the surface of the m-TiO_2, decreasing the surface roughness from 24.8 to 22.5 nm. However, the authors observed that the J-V performance and parameters decreased when two GQD coatings were applied. The Nyquist plot suggested that the reason for this was enhanced recombination. However, it also is possible that excessive amounts of GQDs, which act as electron traps, establish high electron concentrations that effectively reverse the direction of electron diffusion.

Lamanna et al. [79] recently reported a comparison of a two-terminal perovskite/silicon heterojunction (JHT) tandem solar cell, as shown in Figure 4c, with and without GR added to both the m-TiO_2 and c-TiO_2 layers. These data showed that the PCE increased from 24.2% to 26.3%, as shown in Figure 4d, with retention at 25.9% after stabilization (inset). The V_{oc} increased from 1.76 V to 1.80 V, the J_{sc} remained essentially unchanged, and the FF increased from 0.73 to 0.75. The voltage scans showed only marginal hysteresis, with 25.0% (forward) and 26.3% (reverse).

As shown in Figure 4e, the authors [79] also prepared a bifacial PSC of FTO/c-TiO_2/m-TiO_2/perovskite/HTM/ITO configuration; again, the comparison was between PSCs with and without GR added to both the m-TiO_2 and c-TiO_2 layers. These data showed that a PCE increase from 11.3% to 12.6%, a V_{oc} increase from 1.08 V to 1.12 V, a slight J_{sc} decrease from 19.96 mA/cm^2 to 19.85 mA/cm^2, and an FF increase from 0.53 to 0.57. The addition of GR also decreased the extent of hysteresis. voltage scans showed only marginal hysteresis, with 25.0% (forward) and 26.3% (reverse).

4. SnO_2

SnO_2 also has been explored as an ETL since it exhibits excellent optical transmission, a suitable E_g, a relatively low CBM level, and high electron mobility [92–95]. ETLs of compact SnO_2 thin films as planar layers from sol-gel solutions have achieved a maximal PCE of 21.6% [96,97]. SnO_2 has advantages over TiO_2 in the form of lower processing temperatures (55–180 °C) [93,98,99] and the absence of UV-induced degradation [100]. However, surface defects, such as oxygen vacancies, resulting from the synthesis of SnO_2 may hinder electron transfer and reduce the performance of PSCs [101]. GBMs have been added to SnO_2 to passivate surface defects and tune the semiconducting properties, including the electrical conductivity and energy levels [24,26,56,93,98,99].

Hong et al. [26] reported a composite of SnO_2 and nitrogen-doped graphene oxide (NGO) as an ETL in planar n-i-p structure PSCs, where the surface oxygen vacancies were passivated by NGO. Fabrication involved a dispersion of NGO, which acted as an oxidizing agent, and $SnCl_2 \cdot 2H_2O$, which was dissolved in ethanol, after which the spin-coated layer was calcined at 180 °C. A peak PCE of 16.54% was obtained by a PSC with 5 vol% NGO and enhanced V_{oc} and FF of 1.17 V and 0.75, respectively, were determined. The oxidation of Sn^{2+} to Sn^{4+} to form SnO_2 was confirmed by the trends in deconvoluted Sn $3d_{5/2}$ XPS data, as shown in Figure 5a,b, and by the deconvoluted O_{1s} XPS data, as shown in Figure 5c,d. These results demonstrate that GBMs are not limited to chemically passive agents for increased electrical conductivity. They also may act as oxidizing agents, as in NGO, or are reducing agents, as in GR. The SnO_2-NGO ETL exhibited higher electrical conductivity, lower recombination rate, and more efficient charge extraction relative to the SnO_2 ETL.

Xie et al. [56] were the first to report GQDs as additives to SnO_2 in order to overcome the trap states in low-temperature solution-processed (i.e., defective) SnO_2. ETLs modified with 1 wt % GQDs achieved an average PCE of 19.2 ± 1.0% with reduced hysteresis, which was attributed to facilitated electron transport and reduced charge recombination. As shown in Figure 5e, the J-V characteristics for ETL-only devices of Ag/SnO_2/ITO and Ag/SnO_2-GQD/ITO configuration showed that the electrical conductivity under the illumination of the latter was greater than that of the former by a factor of ~20; the same factor was obtained for comparison of the Ag/SnO_2-GQD/ITO configuration for illuminated vs. dark conditions. The improved electrical conductivity was attributed to the role of the GQDs in providing segregated trap states in SnO_2, which accumulate large isolated concentrations of free electrons, thereby acting as localized reservoirs that avoid recombination and facilitate efficient transport of electrons. Kelvin probe force microscopy (KPFM) measurements showed that the E_F of SnO_2-GQD was reduced from 4.35 to 4.01 eV under illumination by simulated sunlight (AM 1.5 G); this moved the E_F closer to that of the CBM of SnO_2, as suggested by Figure 5f. In contrast, equivalent

KPFM measurements for SnO_2 revealed only a small shift in the E_F. These results also indicated that ETLs of SnO_2-GQD exhibited increased V_{oc} relative to that of SnO_2.

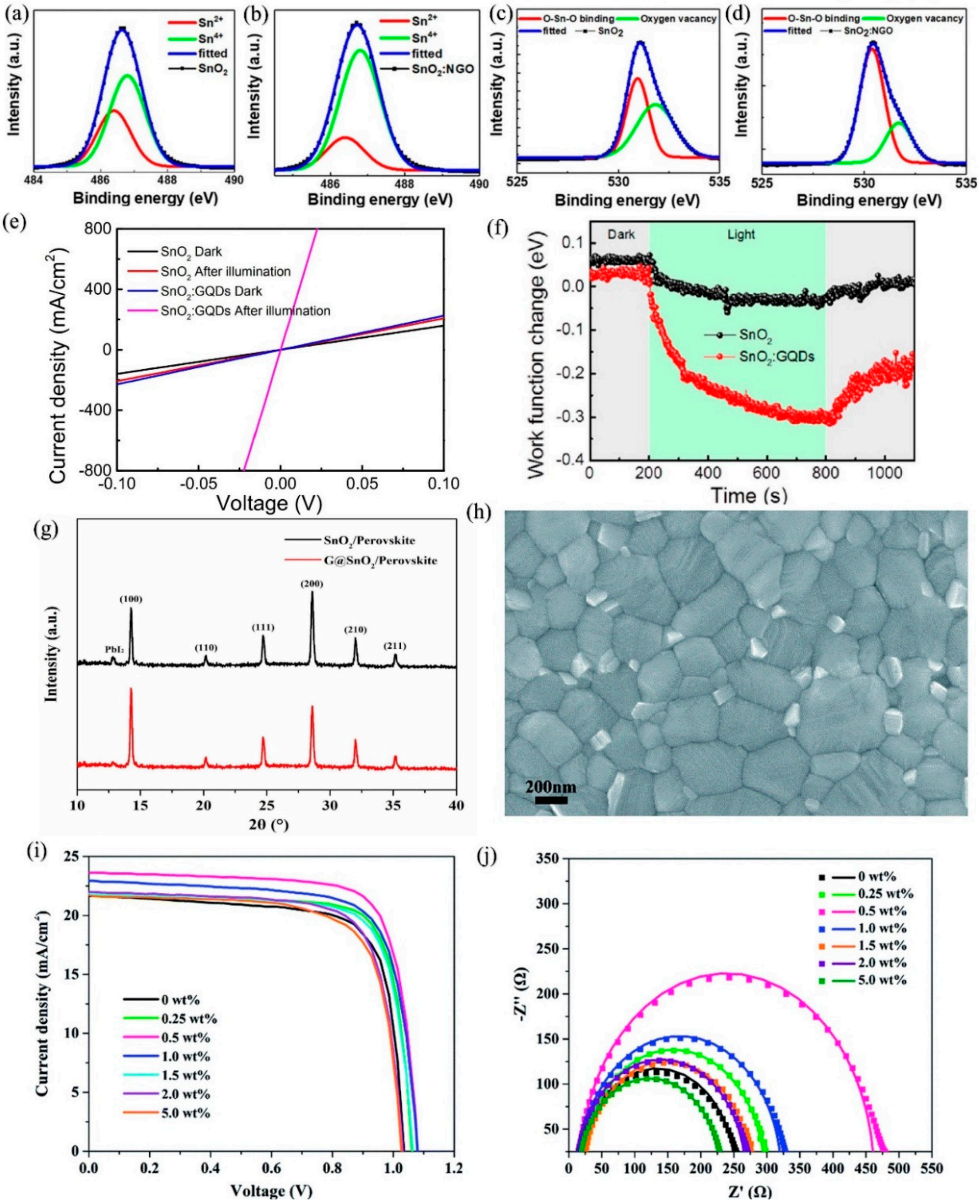

Figure 5. Sn $3d_{5/2}$ XPS spectra for (**a**) SnO_2, (**b**) SnO_2-NGO; O_{1s} XPS spectra for (**c**) SnO_2, (**d**) SnO_2-NGO [26] (republished with permission from American Chemical Society); (**e**) J-V characteristics of the ETL-only devices (Ag/SnO_2/ITO and Ag/SnO_2-GQD/ITO under illuminated (simulated sunlight, the global standard spectrum (AM 1.5 G)) and dark conditions; (**f**) work function changes of ETL-only devices under illuminated and dark conditions [56] (republished with permission from American Chemical Society); (**g**) XRD patterns of perovskite films on SnO_2 and SnO_2-GQD; (**h**) top-view SEM image of perovskite with excess of PbI_2; (**i**) J-V curves and (**j**) Nyquist plots (in the dark at a bias of –1.0 V) of PSCs based on SnO_2 with different GQDs (5 nm Ø) concentrations [24] (republished with permission from Royal Society of Chemistry, conveyed through Copyright Clearance Center, Inc.).

Zhou et al. [24] fabricated spin-coated composites of SnO_2 and GQDs of 5 and 10 nm diameters (SnO_2-5G, SnO_2-10G) as ETLs, which resulted in PCE increases (0.5 wt % GQD additions) from 16.7% to 19.2% and to 18.0%, respectively, in PSCs. The optical and semiconducting properties as a function of GQD Ø and addition level were examined for ETL-only (Au/SnO_2-GQD/FTO) devices and PSCs. Despite the complex stoichiometry of the (Cs, organic)Pb(Br,I)$_3$, Figure 5g shows that the perovskite (deposited on the ETL) was nearly homogeneous. However, these data showed that the amount of grain-boundary PbI_2, as shown in Figure 5h which may passivate defects, is reduced by the GQDs, which also was observed by Sidhik et al. [17].

Concerning the effects of GQD size, the electrical conductivity of the SnO_2-G10 ETL was optimal [24]. However, the recombination rate for the SnO_2-G5 ETL was optimal. However, all the band energy levels decreased with decreasing GQD size.

Concerning the effects of the GQD amount, a high concentration may be harmful to the performance of PSCs [24]. It was observed that the PCE, V_{oc}, and J_{sc} improved with increasing concentration of GQDs up to 0.5 wt %, after which the values of these parameters decreased, as shown in Figure 5i. Charge recombination on the interface also may be worsened with the additions of high concentrations of GQDs, as demonstrated by the Nyquist plots from EIS in Figure 5j. The interfacial recombination resistance (R_{rec}), which corresponds to the diameter of the typical semicircle at low frequency (<103 Hz), decreases when the concentration of GQDs exceeds 0.5 wt %. This indicates inefficient suppression of charge recombination or the possibility of the formation of new charge-recombination centers.

More generally, the utilization of GQDs significantly improved the efficiency of electron extraction and PCEs of the PSCs, with negligible change in the absorption of the perovskite layer. More specifically, the best device (0.5 wt % GQD of 5 nm Ø), with a PCE of 19.2%, exhibited a high V_{oc} of 1.07 V, high J_{sc} of 23.9 mA/cm^2, high FF of 0.75, and reduced hysteresis.

Zhao et al. [60] fabricated ETLs using SnO_2 mixed with graphene-modified by N,N′-bis-[2-(ethanoic acid sodium)]-1,4,5,8-naphthalene diimide (NDI) surfactant. The maximal PCE was 20.2% and the FF also was high at 0.82. The use of graphene-NDI (GR-NDI) facilitated the physisorption across the SnO_2/perovskite interface by van der Waals bonding, which enhanced the semiconducting properties of the ETL. Zhu et al. [25] reported SnO_2-GR as ETLs in PSCs with enhanced electron mobilities and reduced charge recombination, which resulted in highly stable devices with minimal hysteresis under humidity. These characteristics were attributed to the hydrophobicity of graphene and its passivation of the surface trap sites, the former of which would retard the degradation of the perovskite.

5. ZnO

ZnO is a promising semiconducting material that has the potential to replace TiO_2 as the ETL in PSCs. It has an E_g of ~3.3 eV, which is similar to that of TiO_2, but higher bulk electron mobility (~200 cm^2/V s) [102]. Another advantage of ZnO is that it can be synthesized at room-temperature [103,104], which reduces the cost and enables its deposition on flexible devices. However, it has been reported that ZnO-based PSCs exhibit thermal instability, which can lead to severe degradation of the perovskite at temperatures > 100 °C [105]. This degradation has been reported to arise from interaction between the perovskite and the surface hydroxyl groups and residual acetate ligands present on the ZnO [37,105]. Hence, it appears that GBMs may be successful at passivation since their addition has overcome this instability issue, resulting in enhanced electron transport [43,81].

Tavakoli et al. [81] reported using a quasicore-shell structure of ZnO-RGO quantum dots (QDs) as ETL to overcome the thermal instability resulting from the effect of room-temperature hydrolysis of the ZnO nanoparticles on the perovskite. The ZnO-RGO composite layer contributed to the PSC's retention of 90% of its original PCE after 30 days in ambient conditions following encapsulation, which is superior to that of ZnO nanoparticles alone, as shown in Figure 6a. This was attributed to the decreased concentration of hydroxyl groups on the ZnO surface owing to the RGO modification, as confirmed by XPS analysis. Further, improvements in electron transfer efficiency and more rapid electron extraction were additional benefits. Tavakoli et al. [43] reported the deposition of monolayer-GR by low-pressure chemical vapor deposition (LPCVD) on copper foil. The monolayer-GR then was transferred to the top of ZnO ETL as an interfacial layer in order to eliminate the instability caused by ZnO. The result was the achievement of thermal stability through successful hindrance of perovskite decomposition by prevention of direct contact between the two materials. This resulted in long-term stability of the PSCs, as shown in Figure 6b. The GR interlayer also contributed to faster electron extraction and transfer, resulting in PCEs with increased J_{sc} and higher PCE with reduced hysteresis.

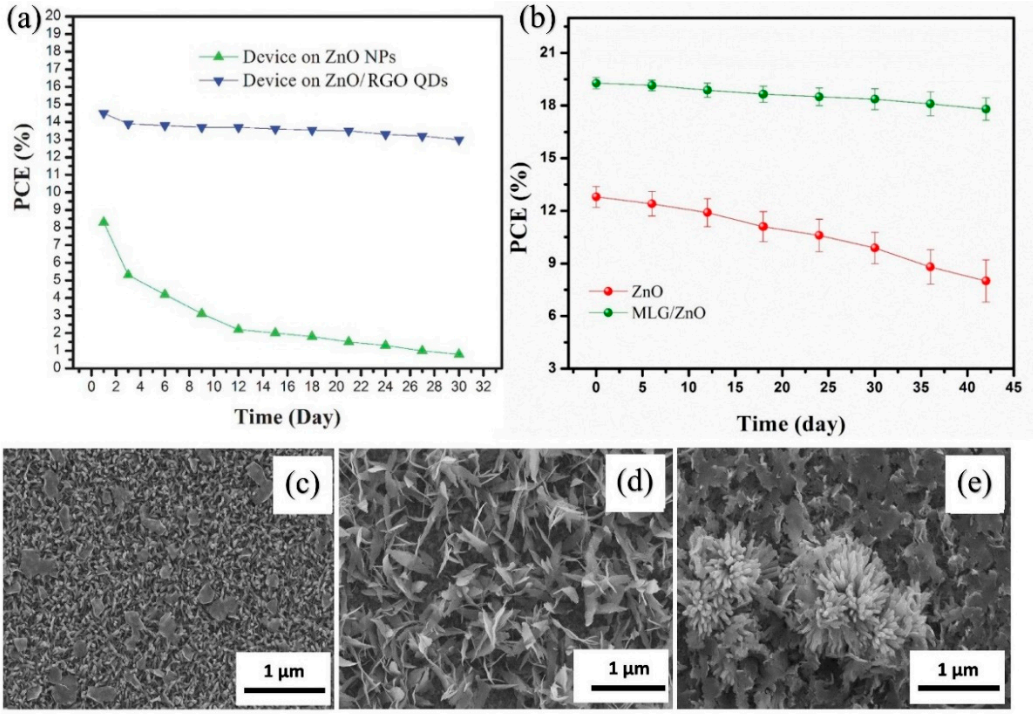

Figure 6. (**a**) Stabilities of PSCs with ETLs of ZnO nanoparticles (NPs) and ZnO/RGO QDs in ambient conditions after encapsulation over 30 days [81] (republished with permission from WILEY); (**b**) Stabilities of PSCs with ETLs of ZnO and ZnO with monolayer-GR (MLG/ZnO) in ambient conditions with 30% humidity over 42 days [43] (republished with permission from the Royal Society of Chemistry); top-view SEM images of ZnO nanorods modified by nitrogen-doped GR at concentration of (**c**) 0.4 wt %, (**d**) 0.8 wt %, (**e**) 1.0 wt % [74] (republished with permission from Elsevier)

GBMs can serve as means for efficient passivation for ZnO ETLs in the forms of both core-shell structures or monolayers, although this would be impacted by the surface chemistry of ZnO, which is highly dependent on the method and chemicals of synthesis. Alternative to these GBMs as semiconducting passivating interlayers are PCBM and polyethylenimine (PEI), which can be deposited by sol-gel [37]. These represent simple and cost-effective materials and methods to passivate ZnO and facilitate electron transfer.

Other reports of GBM-modified ZnO ETLs focused on the improvement of electron transport and the PSC performance. Ahmed et al. [75] reported that ZnO-GO exhibited lower resistivity than ZnO and hence lowered the series resistance of PSCs. Chandrasekhar et al. [76] reported the fabrication of ZnO-GR ETL by spray coating at 150 °C on top of a ZnO compact layer. In comparison to ZnO, ZnO modified with 0.75 wt % GR contributed to improved crystallinity of perovskite thin films while the grain size increased from ~100 nm to ~200–250 nm, with decreased surface roughness. The EQE increased from ~55% to >75%, clearly showing the benefit of GR modification on the semiconducting properties of the PSCs. However, a negative effect from the large concentration of GR (1.0 wt %) was observed in the form of decreased PCE and less quenching in the PL spectra.

Chandrasekhar et al. [74] reported the fabrication of a high-efficiency PSC using an ETL of ZnO modified with nitrogen-doped-GR (NGR). Wurtzite ZnO nanorods were deposited on a ZnO seed layer by chemical bath deposition, followed by high-temperature sintering (350°C). Increasing concentration of NGR was reported to increase both the crystallinity and grain size of the perovskite, the latter of which is shown in Figure 6c–e. Increasing the NGR content to 0.8 wt % caused the PCE to increase from 12.87% to 16.82%, the J_{sc} to increase from 17.38 mA/cm^2 to 21.98 mA/cm^2, the FF to increase from 0.71 to 0.74, the V_{oc} to decrease slightly from 1.04 to 1.02 V, and the PSC hysteresis to disappear. The nanorod arrays on the seed layer were considered to act as a quasimesoporous ETL layer, similar to those observed in TiO_2 that also reduced the hysteresis [89].

Taheri-Ledari et al. [80] reported an HTM-free PSC with a composite ETL of ZnO with RGO and $CuInS_2$ quantum dots that showed good device stability. The RGO was synthesized in situ with ZnO using the hydrothermal method. The addition of RGO, which has a suitable CBM of −4.4 eV, enhanced the electron transfer and contributed to the improvement in the photovoltaic performance of PSCs. A mixture of 80 wt % ZnO + 16 wt % $CuInS_2$ + 4 wt % RGO sintered at 300 °C resulted in a uniform flat microstructure of 3–5 µm grains yielded a high PCE of 15.74%, with good stability.

Finally, ZnO of different nanostructures has been reported to be an effective ETL in the forms of nanoparticles, nanorods, nanowires, nanosheets, and 3D hierarchical structures [87]. However, there is a dearth of data for GQD modification of ZnO structures for ETLs and these GBMs would be expected to be able to make a positive impact on both electron transfer and overall PSC performance.

6. PCBM

Organic materials, such as fullerenes and their derivatives, have been investigated as ETLs in p-i-n type PSCs because they offer simplified fabrication, low-temperature processing, low costs, and feasibility for coatings on flexible substrates [106]. The complex fullerene [6,6]-phenyl-C_{61}-butyric acid methyl ester (PCBM) is an organic ETL material that has been used extensively in PSCs. It has been reported that PCBM passivates the perovskite layer and suppresses hysteresis in PSCs [107,108]. Recently, GBMs have been mixed with PCBM to enhance the photovoltaic properties of PSCs. This effectively improved not only the semiconducting properties of the ETL but also the stability of the devices [70,72].

Yang et al. [70] reported data for PCBM and GQD-modified PCBM (PCBM-GQD), which were ETLs in p-i-n structure PSCs. The use of 0.5 wt % GQD increased the PCE from 14.68% to 17.56%. The electrical conductivity increased from 0.151 mS cm^{-1} to 0.422 mS cm^{-1}. PCBM-GQD also showed enhanced electron extraction, which resulted in higher V_{oc} and FF values. The unsealed PSC also exhibited stability owing to the maintenance of the PCE at ~80% and the FF at ~0.9after 300 h of continuous simulated solar illumination in the air at ~45% relative humidity. In contrast, the reference PSC with PCBM ETL showed a >50% decrease in PCE and a ~30% decrease in FF under the same conditions, as shown in Figure 7a,b. It was suggested that enhanced stability may result from the suppression of the dimerization of PCBM under light exposure through the addition of GQDs.

Kakavelakis et al. [72] reported the performances of RGO-modified PCBM in ETLs in p-i-n structure PSCs, which enhanced the electrical conductivities and stabilized the PCBM/perovskite interface in PSCs. At the optimal concentration of 5 wt % RGO in PCBM, the electrical conductivity increased from 0.109 to 0.495 mS·cm^{-1}, the J_{sc} increased from 20.65 to 22.92 mA/cm^2, and the photo-charging effect during light soaking also reduced. The V_{oc} and FF of the unsealed PSCs showed only very minor changes after 100 h illumination under AM 1.5G simulated solar light, as shown in Figure 7c,d, indicating only minor perovskite degradation and stabilized PCBM/perovskite interface.

Bi et al. [71] reported data for PCBM and PCBM modified with 2 wt % N-doped graphene (PCBM-NGR) in p-i-n structure PSCs of FTO/NiMgLiO/$MAPbI_3$/PCBM-NGR/CQDs/Ag configuration, which showed significant improvements in stability owing to successful hindrance of the diffusion of iodide ions (the natures of 20 nm thickness NiMgLiO and the 10 nm Ø carbon quantum dots (CQDs) were not described). As the NGR nanoparticles exhibited a dimension of ~100 nm Ø, this large size would facilitate passivation and consequent suppression of penetration into the ETL. The long-term stability of sealed PSCs was tested under both illuminated and dark conditions, the results of which are shown in Figure 7e. These data showed that the PSCs with PCBM-NGR ETLs were stable and exhibited PCEs >15% under both conditions. Testing of the ETL-only devices revealed that the PCBM-NGR (relative to PCBM) exhibited superior semiconducting properties and more homogenous nanostructures. The electrical conductivity increased from 4.1 to 23.1 nA (bias 1 V, current through 150 nm ETL film thickness). More rapid electron extraction and slower carrier recombination rates were demonstrated by PL and time-resolved photoluminescence (TRPL). The impact on morphology was characterized by AFM, where fewer PCBM agglomerates and lower roughness were observed, where the roughness decreased from 6 to 1 nm.

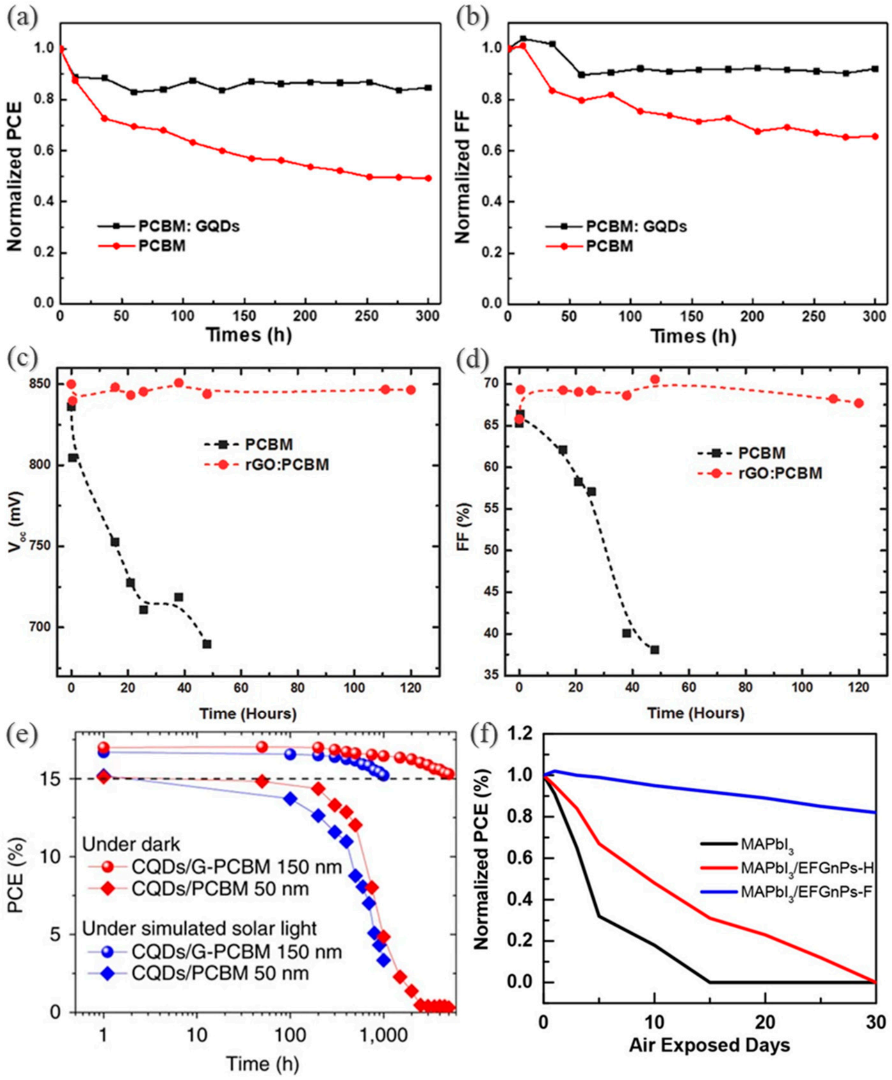

Figure 7. Stabilities of PSCs with ETLs of PCBM and PCBM-GQD under continuous simulated solar illumination in air with ~45% relative humidity [70]: (**a**) Normalized PCE, (**b**) normalized fill factor (FF) (republished with permission from Elsevier); Stabilities of PSCs with ETLs of PCBM and PCBM-RGO under continuous simulated solar illumination in ambient air with ~50% relative humidity [72]: (**c**) Voc, (**d**) FF (republished with permission from Wiley-VCH; (**e**) Stabilities of sealed PSCs under simulated solar light (AM 1.5G) and dark conditions in ambient air [71] (republished with permission from Springer Nature); (**f**) Stabilities of unsealed PSCs under simulated solar light (AM 1.5G) and dark conditions in ambient air with ~50 relative humidity [78] (republished with permission from American Chemical Society).

Kim et al. [78] developed GNPS that were selectively edge-functionalized (EF) with hydrogen (GNP-H) or fluorine (GNP-F) prepared by ball milling of graphite under H_2 or XeF_2 gas. These nanoparticles were dispersed in isopropanol (5 mg/mL) and spin coated on the PCBM layer of p-i-n structure PSCs of ITO/HTM/$MAPBI_3$/PCBM/EF-GNP/Al configuration. The unsealed PSCs with ETLs of GNP-F showed good stability, maintaining 82% of the initial average PCE of 13.4% after 30 days in ambient air with ~50% relative humidity under illuminated (simulated sunlight, AM 1.5G) and dark conditions, as shown in Figure 7f. This excellent stability is attributed to the hydrophobicity of the fluorine, which protected the perovskite layer from moisture.

7. Other ETL Materials

There is only limited information on other ETL materials with GBMs beyond those discussed in the present work. These appear to be limited to reports on ETLs based on Fe_2O_3 [77] and compact $SrTiO_3$ (STO) with mesoporous Al_2O_3 [55].

8. Summary and Outlook

In summary, the present work reviews the major studies of GBM-containing ETLs. The main bases for these components of PSCs are TiO_2, SnO_2, ZnO, and PCBM. Table 1 summarizes PSCs with ETLs modified by GBMs of the highest PCEs. Table 2 provides an extensive summary of the performances of PSCs with GBM-modified ETLs.

GQDs are suitable for addition to the dense microstructures of metal oxide semiconductors, such as TiO_2, SnO_2, and ZnO. The PSC performances using such materials are controlled largely by the size of the GQDs. In contrast, nanoparticles of GR, GO, and RGO, which are larger than GQDs, are more effective in mesoporous microstructures. In this case, the PSC performances are dominated largely by the concentrations of the GBMs rather than the sizes.

A single layer of GBM, typically deposited on the top of the ETL and functioning as an interfacial layer, represents a beneficial configuration for the improvement semiconducting properties of the ETL and hence the charge transfer across the ETL/perovskite interface through passivation of the ETL surface and enhancing interfacial bonding. Since a thin and uniform GBM layer is challenging to deposit using a suspension, vacuum deposition represents a promising method for such deposition.

From examination of the principal reports on GBM-modified ETLs and consideration of the relative merits and shortcomings of these devices, a number of conclusions can be made concerning the role of the GBMs. Owing to their outstanding semiconducting properties, their addition to ETLs can be expected to offer several advantages:

- Enhanced electron transport from increased electrical conductivity and electron mobility of the ETL;
- Enhanced electron transport from improved ETL/perovskite effective interfacial apposition;
- Enhanced J-V characteristics and parameters of PSCs largely owing to more effective electron extraction and transport deriving from the ETLs;
- Enhanced J-V characteristics of PSCs through reduced hysteresis owing to leveraging of surface trap sites created by GBMs;
- Potential tuning of the E_g and the energy levels to optimise charge transfer to and from the ETL;
- Enhanced device stability (i.e., protection of the perovskite from water vapour—hydrophobicity) from passivation of the ETL at the ETL/perovskite interface;
- Enhanced device stability through prevention of alteration of perovskite by inhibition of diffusion and counter-diffusion of mobile ions across the ETL/perovskite interface;
- Enhanced device stability through increased crystallinity of perovskite from the action of GBMs as nucleating agents.

Table 1. Summary of reports of PSCs with the highest PCEs containing ETLs with GBMs.

ETL Material	Device Structure	PCE (%)	V_{OC} (V)	J_{SC} (mA/cm^2)	FF	ΔPCE (Relative to Pristine ETL) (%)	Ref.
SnO_2 + GQDs	ITO/SnO_2-GQDs/$MAPbCl_{3-x}I_x$/Spiro-OMeTAD/Ag	21.10	1.11	24.40	0.78	+13	[19]
m-TiO_2 + RGO	FTO/c-TiO_2/m-TiO_2-RGO/$(FAPbI_3)_{0.85}(MAPbBr_3)_{0.15}$/Spiro-OMeTAD/Au	19.54	1.11	21.98	0.80	+ 3	[65]
c-TiO_2 + GQDs	FTO/c-TiO_2-GQDs/$MAPbI_3$/Spiro-OMeTAD/Au	19.11	1.12	22.47	0.76	+11	[18]
PCBM + GQDs	ITO/PCBM-GQDs/$MAPbI_3$/Spiro-OMeTAD/Au	17.56	1.09	22.03	0.73	+20	[70]
ZnO + GR	FTO/ZnO-GR/Perovskite/Spiro-OMeTAD/Au	19.81	1.12	22.71	0.77	+43	[43]
STO + (m-Al_2O_3 + GR)	FTO/$Sr_{0.05}Ti_{0.95}O_3$/m-Al_2O_3-GR/$MAPbI_{3-x}Cl_x$ + Ag-RGO/Spiro-OMeTAD/Au	20.58	1.06	25.75	0.76	+29	[55]
α-Fe_2O_3 + GQDs	FTO/α-Fe_2O_3-GQDs/$MAPbI_3$ + GQDs/GQDs/Spiro-OMeTAD/Au	19.2	1.03	23.50	0.79	+37	[77]

GR = graphene; GO = graphene oxide; RGO = reduced graphene oxide; GQDs = graphene quantum dots. SC = spin coating; EPD = electrophoretic deposition; LPCVD = low-pressure chemical vapor deposition $MAPbCl_{3-x}I_3$, $MAPbI_3$, $FA_{0.75}MA_{0.15}Cs_{0.1}PbI_{2.65}Br_{0.35}$, $RbCsFAMAI_3$; $(FAPbI_3)_{0.85}(MAPbBr_3)_{0.1}$, $FAPbI_3)_{1-x}(MAPbBr_3)$, $CsFAMAI_3$ = mixed halide perovskites. Spiro-OMeTAD = 2,2′,7,7′-tetrakis(N,N-di-p-methoxyphenyl-amine)9,9′-spirobifluorene; c-TiO_2 = compact TiO_2; m-TiO_2 = mesoporous TiO_2; m-Al_2O_3 = mesoporous Al_2O_3; NDI = N,N′-bis-[2-(ethanoic acid sodium)]-1,4,5,8-naphthalene diimide; NGR = nitrogen-doped graphene; NiMgLiO = Mg and Li doped NiO; PCBM = phenyl-C_{61}-butyric acid methyl ester; CQD = carbon quantum dots; PEDOT:PSS = poly(ethylene-dioxythiophene doped with poly(4-styrenesulfonate)); EFGR-F = fluorine edged functionalized graphene; Ag-RGO = Ag-reduced graphene oxide; GO-Li = graphene oxide neutralized by lithium bis(trifluoromethylsulphonyl)imide (Li-TFSI); NF = nanofiber; PFN = poly[(9,9-bis(3′-(N,N-dimethylamino)propyl)-2,7-fluorene)-alt-2,7-(9,9-dioctylfluorene); PET = polyethylene terephthalate; APTES = 3-aminopropyl triethoxysilane; PTAA = poly(triarylamine); NSGQDs = nitrogen and sulfur co-doped GQDs.

Table 2. Summary of performance of PSCs with GBM-modified ETLs.

GBM	Dosage	Synthesis	Device Structure	PCE (%)	V_{OC} (V)	J_{SC} (mA/cm^2)	FF	Ref.
GR	2 wt %	SC	FTO/c-TiO_2/m-TiO_2-GR/$MAPbI_3$/Spiro-OMeTAD/Au	19.23	1.00	23.67	0.80	[17]
GR	1 vol %	SC	FTO/c-TiO_2/m-TiO_2-GR/$MAPbI_3$/Spiro-OMeTAD/Au	14.60	1.03	22.95	0.69	[66]
GR	1 vol %	SC	FTO/c-TiO_2/m-TiO_2-GR/$MAPbI_3$/Spiro-OMeTAD/Au	16.00	1.04	20.99	0.73	[20]
GR	0.15 & 1.3 wt %	SC	FTO/c-TiO_2-GR/m-TiO_2-GR/$MAPbI_3$/Spiro-OMeTAD/Ag	17.69	1.05	22.98	0.73	[27]
GR	0.6 wt %	SC	FTO/c-TiO_2-GR/Al_2O_3/$MAPbI_{3-x}Cl_x$/Spiro-OMeTAD/Ag	15.60	1.04	21.90	0.73	[63]
GR	Single layer	EPD	FTO/c-TiO_2/porous GR/$MAPbI_3$/Spiro-OMeTAD/Au	17.20	1.05	22.80	0.72	[109]
GR	5 vol %	SC	ITO/SnO_2-NDI-GR/$FA_{0.75}MA_{0.15}Cs_{0.1}PbI_{2.65}Br_{0.35}$/Spiro-OMeTAD/Ag	20.16	1.08	22.66	0.82	[60]
GR	1 vol %	SC	FTO/SnO_2-GR/$MAPbI_3$/Spiro-OMeTAD/Au	18.11	1.09	23.06	0.72	[25]
GR	Single layer	LPCVD	FTO/ZnO-GR/FAMAPbI$_3$/Spiro-OMeTAD/Au	19.81	1.12	22.71	0.77	[43]
GR	0.8 wt %	Hydrothermal	FTO/ZnO-NGR/$MAPbI_3$/Spiro-OMeTAD/Ag	16.82	1.01	21.98	0.77	[74]
GR	0.75 wt %	Spray coating	FTO/ZnO-GR/$MAPbI_3$/Spiro-OMeTAD/Ag	10.34	0.93	19.97	0.56	[76]
GR	2 wt %	SC	FTO/NiMgLiO/$MAPbI_3$/NGR-PCBM/CQDs/Ag	15.80	1.07	19.69	0.75	[71]

Table 2. *Cont.*

GBM	Dosage	Synthesis	Device Structure	PCE (%)	V_{OC} (V)	J_{SC} (mA/cm^2)	FF	Ref.
GR	Single layer	SC	ITO/PEDOT:PSS/$MAPbI_3$/PCBM/EFGR-F/Al	14.30	0.98	18.50	0.78	[78]
GR	No info.	SC	FTO/$Sr_{0.05}Ti_{0.95}O_3$/m-Al_2O_3-GR/$MAPbI_{3-x}Cl_x$ + Ag-RGO/Spiro-OMeTAD/Au	20.58	1.06	25.75	0.76	[55]
GO	Single layer	SC	FTO/c-TiO_2/m-TiO_2/GO-Li/$MAPbI_3$/Spiro-OMeTAD/Au	15.20	1.02	22.51	0.65	[20]
GO	5 vol%	SC	ITO/SnO_2-NGO/$RbCsFAMAI_3$/Spiro-OMeTAD/Ag	16.54	1.17	19.28	0.71	[26]
RGO	No info.	SC	FTO/c-TiO_2/m-TiO_2-RGO/$(FAPbI_3)_{0.85}(MAPbBr_3)_{0.15}$/Spiro-OMeTAD/Au	19.54	1.11	21.98	0.80	[65]
RGO	No info.	Electrospinning	FTO/c-TiO_2/TiO_2-RGO NF/$(FAPbI_3)_{0.85}(MAPbBr_3)_{0.15}$/Spiro-OMeTAD/Au	17.66	1.07	22.16	0.75	[68]
RGO	0.4 vol %	SC	FTO/c-TiO_2/m-TiO_2-RGO/$MAPbI_3$/Spiro-OMeTAD/Ag	14.50	0.93	22.00	0.71	[23]
RGO	Core-shell	Sol-gel	FTO/ZnO-RGO/$MAPbI_3$/Spiro-OMeTAD/Ag	15.20	1.03	21.70	0.68	[81]
RGO	5 wt %	SC	FTO/ZnO-RGO/$MAPbI_3$/Spiro-OMeTAD/Au	11.97	1.00	19.95	0.61	[80]
RGO	5 vol %	SC	ITO/PEDOT:PSS/$MAPbI_{3-x}Cl_x$/PCBM-RGO/PFN/Ag	14.51	0.94	23.52	0.65	[72]
GQDs	1 mg/mL	SC	FTO/c-TiO_2/m-TiO_2-GQDs/$(FAPbI_3)_{1-x}(MAPbBr_3)$/Spiro-OMeTAD/Au	20.45	1.08	24.92	0.76	[39]
GQDs	3 mg/mL	SC	FTO/c-TiO_2-GQDs/$MAPbI_3$/Spiro-OMeTAD/Au	19.11	1.12	22.47	0.76	[18]
GQDs	No info.	SC	ITO/SnO_2-GQD/$MAPbI_{3-x}Cl_x$/Spiro-OMeTAD/Ag	21.10	1.11	24.40	0.78	[19]
GQDs	1 wt %	SC	ITO/SnO_2-GQD/$MAPbI_3$/Spiro-OMeTAD/Au	20.31	1.13	23.05	0.78	[56]
GQDs	0.5 wt %	SC	ITO/SnO_2-GQD/$CsFAMAI_3$/Spiro-OMeTAD/Au	19.60	1.08	23.50	0.77	[24]
GQDs	0.5 wt %	SC	ITO/PCBM-GQD/$MAPbI_3$/Spiro-OMeTAD/Au	17.56	1.09	22.03	0.73	[70]
GQDs	2.5 mg/L	SC	PET/APTES/GR/PCBM-GQD/$MAPbI_3$/PTAA/Au	16.41	1.07	20.75	0.74	[73]
GQDs	0.5 mg/mL	SC	FTO/α-Fe_2O_3-NSGQDs/$MAPbI_3$ + NSGQDs/NSGQDs/Spiro-OMeTAD/Au	19.2	1.03	23.50	0.79	[77]
Mixed	N/A	SC	FTO/c-TiO_2/m-TiO_2-GR/GO-Li/$MAPbI_3$/Spiro-OMeTAD/Au	16.20	1.03	22.85	0.69	[20]
Mixed	N/A	SC	FTO/c-TiO_2/m-TiO_2-GR/GO-Li/$MAPbI_3$/Spiro-OMeTAD/Au	12.6 (50 cm^2 module)				[61]

GR = graphene; GO = graphene oxide; RGO = reduced graphene oxide; GQDs = graphene quantum dots. SC = spin coating; EPD = electrophoretic deposition; LPCVD = low-pressure chemical vapor deposition $MAPbCl_{3-x}I_3$, $MAPbI_3$, $FA_{0.75}MA_{0.15}Cs_{0.1}PbI_{2.65}Br_{0.35}$, $RbCsFAMAI_3$; $(FAPbI_3)_{0.85}(MAPbBr_3)_{0.1}$, $FAPbI_3)_{1-x}(MAPbBr_3)$, $CsFAMAI_3$ = mixed halide perovskites. Spiro-OMeTAD = 2,2′,7,7′-tetrakis(N,N-di-p-methoxyphenyl-amine)9,9′-spirobifluorene; c-TiO_2 = compact TiO_2; m-TiO_2 = mesoporous TiO_2; m-Al_2O_3 = mesoporous Al_2O_3; NDI = N,N′-bis-[2-(ethanoic acid sodium)]-1,4,5,8-naphthalene diimide; NGR = nitrogen-doped graphene; NiMgLiO = Mg and Li doped NiO; PCBM = phenyl-C_{61}-butyric acid methyl ester; CQD = carbon quantum dots; PEDOT:PSS = poly(ethylene-dioxythiophene doped with poly(4-styrenesulfonate)); EFGR-F = fluorine edged functionalized graphene; Ag-RGO = Ag-reduced graphene oxide; GO-Li = graphene oxide neutralized by lithium bis(trifluoromethylsulphonyl)imide (Li-TFSI); NF = nanofiber; PFN = poly[(9,9-bis(3′-(N,N-dimethylamino)propyl)-2,7-fluorene)-alt-2,7-(9,9-dioctylfluorene); PET = polyethylene terephthalate; APTES = 3-aminopropyl triethoxysilane; PTAA = poly(triarylamine); NSGQDs = nitrogen and sulfur co-doped GQDs.

These multiple factors are responsible for the variable effects of GBM size, amount, and distribution on the performance through alteration of the nanostructure and associated features, including the impact of surface coverage and agglomeration on the electron diffusion path lengths and directions, interfacial electron transfer, and electron mean free path. Ultimately, these factors are directly relevant to the probability that the kinetics of charge transport are extended such that charge recombination can take place.

Although GBMs generally are assumed to be physisorbed on nanoparticle surfaces, the observation of chemical effects suggests that it may be possible to chemisorb GBMs. This outcome would be likely to generate robust nanostructures of enhanced electron transfer capacities. Modification of the surfaces of GBMs by, for example, redox, functionalization, or intercalation, also represents a strategy to improve the stability of PSCs.

The near-universal method of fabrication of these PSCs is spin coating, which is simple, rapid, and inexpensive while yielding high-quality layered nanostructures. The raw materials include both dispersions and sol-gel solutions. However, there may be size limitations to spin coating, where the film consistency would tend to decrease with increasing size and the cost would increase similarly. Emerging methods, such as 3D printing, screen printing, atomic layer deposition (ALD), and cold-spray deposition, offer promising trajectories.

Author Contributions: X.D. undertook the research, prepared the first draft of the manuscript, and contributed to all subsequent drafts; P.K. contributed to all preliminary drafts; C.C.S. prepared the penultimate and final drafts on the basis of the preliminary drafts; J.L. contributed to all preliminary drafts; J.S.Y. supervised the research and contributed to all preliminary drafts. All authors have read and agreed to the published version of the manuscript.

Funding: This research received no external funding.

Acknowledgments: This research is/was supported by an Australian Government Research Training Program (RTP) Scholarship. J.L. acknowledges the supports by research fund of Chungnam National University. J. Yun acknowledges the Australian Centre for Advanced Photovoltaics (ACAP) that encompasses the Australian-based activities of the Australia-US Institute for Advanced Photovoltaics (AUSIAPV) and is supported by the Australian Government through the Australian Renewable Energy Agency (ARENA). Responsibility for the views, information or advice expressed herein is not accepted by the Australian Government. The authors would like to thank Mr. Zizhen Zhou for assistance with preparation of Figure 1a.

Conflicts of Interest: The authors declare no conflict of interest.

References

1. Jean, J.; Brown, P.R.; Jaffe, R.L.; Buonassisi, T.; Bulović, V. Pathways for Solar Photovoltaics. *Energy Environ. Sci.* **2015**, *8*, 1200–1219. [CrossRef]
2. Green, M.A.; Dunlop, E.D.; Hohl-Ebinger, J.; Yoshita, M.; Kopidakis, N.; Ho-Baillie, A.W.Y. Solar Cell Efficiency Tables (Version 55). *Prog. Photovolt. Res. Appl.* **2020**, *28*, 3–15. [CrossRef]
3. Li, Z.; Klein, T.R.; Kim, D.H.; Yang, M.; Berry, J.J.; van Hest, M.F.A.M.; Zhu, K. Scalable Fabrication of Perovskite Solar Cells. *Nat. Rev. Mater.* **2018**, *3*, 18017. [CrossRef]
4. NREL. Best Research-Cell Efficiencies. Available online: https://www.nrel.gov/pv/assets/pdfs/best-research-cell-efficiencies.20200925.pdf (accessed on 21 October 2020).
5. Kojima, A.; Teshima, K.; Shirai, Y.; Miyasaka, T. Organometal Halide Perovskites as Visible-Light Sensitizers for Photovoltaic Cells. *J. Am. Chem. Soc.* **2009**, *131*, 6050–6051. [CrossRef] [PubMed]
6. Hirasawa, M.; Ishihara, T.; Goto, T. Exciton Features in 0-, 2-, and 3-Dimensional Networks of $[PbI_6]^{4-}$ Octahedra. *J. Phys. Soc. Jpn.* **1994**, *63*, 3870–3879. [CrossRef]
7. Tanaka, K.; Takahashi, T.; Ban, T.; Kondo, T.; Uchida, K.; Miura, N. Comparative Study on the Excitons in Lead-Halide-Based Perovskite-Type Crystals $CH_3NH_3PbBr_3$ $CH_3NH_3PbI_3$. *Solid State Commun.* **2003**, *127*, 619–623. [CrossRef]
8. Filip, M.R.; Eperon, G.E.; Snaith, H.J.; Giustino, F. Steric Engineering of Metal-Halide Perovskites with Tunable Optical Band Gaps. *Nat. Commun.* **2014**, *5*, 5757. [CrossRef] [PubMed]
9. Noh, J.H.; Im, S.H.; Heo, J.H.; Mandal, T.N.; Seok, S.I. Chemical Management for Colorful, Efficient, and Stable Inorganic–Organic Hybrid Nanostructured Solar Cells. *Nano Lett.* **2013**, *13*, 1764–1769. [CrossRef]

10. Dong, Q.; Fang, Y.; Shao, Y.; Mulligan, P.; Qiu, J.; Cao, L.; Huang, J. Electron-Hole Diffusion Lengths > 175 µm in Solution-Grown $CH_3NH_3PbI_3$ Single Crystals. *Science* **2015**, *347*, 967–970. [CrossRef]
11. Stranks, S.D.; Eperon, G.E.; Grancini, G.; Menelaou, C.; Alcocer, M.J.P.; Leijtens, T.; Herz, L.M.; Petrozza, A.; Snaith, H.J. Electron-Hole Diffusion Lengths Exceeding 1 Micrometer in an Organometal Trihalide Perovskite Absorber. *Science* **2013**, *342*, 341–344. [CrossRef]
12. Steirer, K.X.; Schulz, P.; Teeter, G.; Stevanovic, V.; Yang, M.; Zhu, K.; Berry, J.J. Defect Tolerance in Methylammonium Lead Triiodide Perovskite. *ACS Energy Lett.* **2016**, *1*, 360–366. [CrossRef]
13. Motta, C.; El-Mellouhi, F.; Sanvito, S. Charge Carrier Mobility in Hybrid Halide Perovskites. *Sci. Rep.* **2015**, *5*, 12746. [CrossRef] [PubMed]
14. Ono, L.K.; Juarez-Perez, E.J.; Qi, Y. Progress on Perovskite Materials and Solar Cells with Mixed Cations and Halide Anions. *ACS Appl. Mater. Interfaces* **2017**, *9*, 30197–30246. [CrossRef] [PubMed]
15. Leijtens, T.; Lauber, B.; Eperon, G.E.; Stranks, S.D.; Snaith, H.J. The Importance of Perovskite Pore Filling in Organometal Mixed Halide Sensitized TiO_2-Based Solar Cells. *J. Phys. Chem. Lett.* **2014**, *5*, 1096–1102. [CrossRef] [PubMed]
16. Juarez-Perez, E.J.; Wuβler, M.; Fabregat-Santiago, F.; Lakus-Wollny, K.; Mankel, E.; Mayer, T.; Jaegermann, W.; Mora-Sero, I. Role of the Selective Contacts in the Performance of Lead Halide Perovskite Solar Cells. *J. Phys. Chem. Lett.* **2014**, *5*, 680–685. [CrossRef]
17. Sidhik, S.; Panikar, S.S.; Pérez, C.R.; Luke, T.L.; Carriles, R.; Carrera, S.C.; De la Rosa, E. Interfacial Engineering of TiO_2 by Graphene Nanoplatelets for High-Efficiency Hysteresis-Free Perovskite Solar Cells. *ACS Sustain. Chem. Eng.* **2018**, *6*, 15391–15401. [CrossRef]
18. Ryu, J.; Lee, J.W.; Yu, H.; Yun, J.; Lee, K.; Lee, J.; Hwang, D.; Kang, J.; Kim, S.K.; Jang, J. Size Effects of A Graphene Quantum Dot Modified-Blocking TiO_2 Layer for Efficient Planar Perovskite Solar Cells. *J. Mater. Chem. A* **2017**, *5*, 16834–16842. [CrossRef]
19. Pang, S.; Zhang, C.; Zhang, H.; Dong, H.; Chen, D.; Zhu, W.; Xi, H.; Chang, J.; Lin, Z.; Zhang, J.; et al. Boosting Performance Of Perovskite Solar Cells with Graphene Quantum Dots Decorated SnO_2 Electron Transport Layers. *Appl. Surf. Sci.* **2020**, *507*, 145099. [CrossRef]
20. Biccari, F.; Gabelloni, F.; Burzi, E.; Gurioli, M.; Pescetelli, S.; Agresti, A.; Del Rio Castillo, A.E.; Ansaldo, A.; Kymakis, E.; Bonaccorso, F.; et al. Graphene-based Electron Transport Layers in Perovskite Solar Cells: A Step-up for an Efficient Carrier Collection. *Adv. Energy Mater.* **2017**, *7*, 1701349. [CrossRef]
21. Ball, J.M.; Lee, M.M.; Hey, A.; Snaith, H.J. Low-Temperature Processed Meso-superstructured to Thin-Film Perovskite Solar Cells. *Energy Environ. Sci.* **2013**, *6*, 1739–1743. [CrossRef]
22. Salim, T.; Sun, S.; Abe, Y.; Krishna, A.; Grimsdale, A.C.; Lam, Y.M. Perovskite-Based Solar Cells: Impact of Morphology and Device Architecture on Device Performance. *J. Mater. Chem. A* **2015**, *3*, 8943–8969. [CrossRef]
23. Han, G.S.; Song, Y.H.; Jin, Y.U.; Lee, J.-W.; Park, N.-G.; Kang, B.K.; Lee, J.-K.; Cho, I.S.; Yoon, D.H.; Jung, H.S. Reduced Graphene Oxide/Mesoporous TiO_2 Nanocomposite Based Perovskite Solar Cells. *ACS Appl. Mater. Interfaces* **2015**, *7*, 23521–23526. [CrossRef] [PubMed]
24. Zhou, Y.; Yang, S.; Yin, X.; Han, J.; Tai, M.; Zhao, X.; Chen, H.; Gu, Y.; Wang, N.; Lin, H. Enhancing Electron Transport via Graphene Quantum Dot/SnO_2 Composites for Efficient and Durable Flexible Perovskite Photovoltaics. *J. Mater. Chem. A* **2019**, *7*, 1878–1888. [CrossRef]
25. Zhu, M.; Liu, W.; Ke, W.; Xie, L.; Dong, P.; Hao, F. Graphene-Modified Tin Dioxide for Efficient Planar Perovskite Solar Cells with Enhanced Electron Extraction and Reduced Hysteresis. *ACS Appl. Mater. Interfaces* **2019**, *11*, 666–673. [CrossRef]
26. Hong, J.A.; Jung, E.D.; Yu, J.C.; Kim, D.W.; Nam, Y.S.; Oh, I.; Lee, E.; Yoo, J.-W.; Cho, S.; Song, M.H. Improved Efficiency of Perovskite Solar Cells Using a Nitrogen-Doped Graphene-Oxide-Treated Tin Oxide Layer. *ACS Appl. Mater. Interfaces* **2019**. [CrossRef] [PubMed]
27. Meng, X.; Cui, X.; Rager, M.; Zhang, S.; Wang, Z.; Yu, J.; Harn, Y.W.; Kang, Z.; Wagner, B.K.; Liu, Y.; et al. Cascade Charge Transfer Enabled by Incorporating Edge-Enriched Graphene Nanoribbons for Mesostructured Perovskite Solar Cells with Enhanced Performance. *Nano Energy* **2018**, *52*, 123–133. [CrossRef]
28. Wang, J.; Qin, M.; Tao, H.; Ke, W.; Chen, Z.; Wan, J.; Qin, P.; Xiong, L.; Lei, H.; Yu, H.; et al. Performance Enhancement of Perovskite Solar Cells with Mg-Doped TiO_2 Compact Film as the Hole-Blocking Layer. *Appl. Phys. Lett.* **2015**, *106*, 121104. [CrossRef]

29. Xiong, L.; Qin, M.; Yang, G.; Guo, Y.; Lei, H.; Liu, Q.; Ke, W.; Tao, H.; Qin, P.; Li, S.; et al. Performance Enhancement of High Temperature SnO_2-Based Planar Perovskite Solar Cells: Electrical characterization and understanding of the mechanism. *J. Mater. Chem. A* **2016**, *4*, 8374–8383. [CrossRef]
30. Tavakoli, M.M.; Yadav, P.; Tavakoli, R.; Kong, J. Surface Engineering of TiO_2 ETL for Highly Efficient and Hysteresis-Less Planar Perovskite Solar Cell (21.4%) with Enhanced Open-Circuit Voltage and Stability. *Adv. Energy Mater.* **2018**, *8*, 1800794. [CrossRef]
31. Han, G.S.; Chung, H.S.; Kim, B.J.; Kim, D.H.; Lee, J.W.; Swain, B.S.; Mahmood, K.; Yoo, J.S.; Park, N.-G.; Lee, J.H.; et al. Retarding Charge Recombination in Perovskite Solar Cells Using Ultrathin MgO-Coated TiO_2 Nanoparticulate Films. *J. Mater. Chem. A* **2015**, *3*, 9160–9164. [CrossRef]
32. Liu, D.; Li, S.; Zhang, P.; Wang, Y.; Zhang, R.; Sarvari, H.; Wang, F.; Wu, J.; Wang, Z.; Chen, Z.D. Efficient Planar Heterojunction Perovskite Solar Cells with Li-Doped Compact TiO_2 Layer. *Nano Energy* **2017**, *31*, 462–468. [CrossRef]
33. Park, M.; Kim, J.-Y.; Son, H.J.; Lee, C.-H.; Jang, S.S.; Ko, M.J. Low-Temperature Solution-Processed Li-Doped SnO_2 as an Effective Electron Transporting Layer for High-Performance Flexible and Wearable Perovskite Solar Cells. *Nano Energy* **2016**, *26*, 208–215. [CrossRef]
34. Ke, W.; Zhao, D.; Xiao, C.; Wang, C.; Cimaroli, A.J.; Grice, C.R.; Yang, M.; Li, Z.; Jiang, C.-S.; Al-Jassim, M.; et al. Cooperative Tin Oxide Fullerene Electron Selective Layers for High-Performance Planar Perovskite Solar Cells. *J. Mater. Chem. A* **2016**, *4*, 14276–14283. [CrossRef]
35. Dong, Q.; Ho, C.H.Y.; Yu, H.; Salehi, A.; So, F. Defect Passivation by Fullerene Derivative in Perovskite Solar Cells with Aluminum-Doped Zinc Oxide as Electron Transporting Layer. *Chem. Mater.* **2019**, *31*, 6833–6840. [CrossRef]
36. Wang, J.; Datta, K.; Weijtens, C.H.L.; Wienk, M.M.; Janssen, R.A.J. Insights into Fullerene Passivation of SnO_2 Electron Transport Layers in Perovskite Solar Cells. *Adv. Funct. Mater.* **2019**, *29*, 1905883. [CrossRef]
37. Cheng, Y.; Yang, Q.-D.; Xiao, J.; Xue, Q.; Li, H.-W.; Guan, Z.; Yip, H.-L.; Tsang, S.-W. Decomposition of Organometal Halide Perovskite Films on Zinc Oxide Nanoparticles. *ACS Appl. Mater. Interfaces* **2015**, *7*, 19986–19993. [CrossRef] [PubMed]
38. Kegelmann, L.; Wolff, C.M.; Awino, C.; Lang, F.; Unger, E.L.; Korte, L.; Dittrich, T.; Neher, D.; Rech, B.; Albrecht, S. It Takes Two to Tango—Double-Layer Selective Contacts in Perovskite Solar Cells for Improved Device Performance and Reduced Hysteresis. *ACS Appl. Mater. Interfaces* **2017**, *9*, 17245–17255. [CrossRef] [PubMed]
39. Shen, D.; Zhang, W.; Xie, F.; Li, Y.; Abate, A.; Wei, M. Graphene Quantum Dots Decorated TiO_2 Mesoporous Film as an Efficient Electron Transport Layer for High-Performance Perovskite Solar Cells. *J. Power Sources* **2018**, *402*, 320–326. [CrossRef]
40. Georgakilas, V.; Otyepka, M.; Bourlinos, A.B.; Chandra, V.; Kim, N.; Kemp, K.C.; Hobza, P.; Zboril, R.; Kim, K.S. Functionalization of Graphene: Covalent and Non-Covalent Approaches, Derivatives and Applications. *Chem. Rev.* **2012**, *112*, 6156–6214. [CrossRef] [PubMed]
41. Liu, X.; Zhang, Y.; Shi, L.; Liu, Z.; Huang, J.; Yun, J.S.; Zeng, Y.; Pu, A.; Sun, K.; Hameiri, Z.; et al. Exploring Inorganic Binary Alkaline Halide to Passivate Defects in Low-Temperature-Processed Planar-Structure Hybrid Perovskite Solar Cells. *Adv. Energy Mater.* **2018**, *8*, 1800138. [CrossRef]
42. Ryu, S.; Seo, J.; Shin, S.S.; Kim, Y.C.; Jeon, N.J.; Noh, J.H.; Seok, S.I. Fabrication of Metal-Oxide-Free $CH_3NH_3PbI_3$ Perovskite Solar Cells Processed at Low Temperature. *J. Mater. Chem. A* **2015**, *3*, 3271–3275. [CrossRef]
43. Tavakoli, M.M.; Tavakoli, R.; Yadav, P.; Kong, J. A Graphene/ZnO Electron Transfer Layer Together with Perovskite Passivation Enables Highly Efficient and Stable Perovskite Solar Cells. *J. Mater. Chem. A* **2019**, *7*, 679–686. [CrossRef]
44. Petridis, C.; Kakavelakis, G.; Kymakis, E. Renaissance of Graphene-Related Materials in Photovoltaics due to the Emergence of Metal Halide Perovskite Solar Cells. *Energy Environ. Sci.* **2018**, *11*, 1030–1061. [CrossRef]
45. Acik, M.; Darling, S.B. Graphene in Perovskite Solar Cells: Device Design, Characterization and Implementation. *J. Mater. Chem. A* **2016**, *4*, 6185–6235. [CrossRef]
46. Lim, E.L.; Yap, C.C.; Jumali, M.H.H.; Teridi, M.A.M.; Teh, C.H. A Mini Review: Can Graphene Be a Novel Material for Perovskite Solar Cell Applications? *Nano Micro Lett.* **2017**, *10*, 27. [CrossRef] [PubMed]
47. Chen, W.; Lv, G.; Hu, W.; Li, D.; Chen, S.; Dai, Z. Synthesis and Applications of Graphene Quantum Dots: A Review. *Nanotechnol. Rev.* **2018**, *7*, 157. [CrossRef]

48. Dreyer, D.R.; Park, S.; Bielawski, C.W.; Ruoff, R.S. The Chemistry Of Graphene Oxide. *Chem. Soc. Rev.* **2010**, *39*, 228–240. [CrossRef]
49. Pei, S.; Cheng, H.-M. The reduction of graphene oxide. *Carbon* **2012**, *50*, 3210–3228. [CrossRef]
50. Sorrell, C.C.; Taib, H.; Palmer, T.C.; Peng, F.; Xia, Z.M.; Wei, M. Hydroxyapatite and Other Biomedical Coatings by Electrophoretic Deposition. In *Biological and Biomedical Coatings Handbook: Processing and Characterization*; Zhang, S., Ed.; CRC Press-Taylor & Francis Group: Boca Raton, FL, USA, 2011; pp. 81–135.
51. Yan, K.; Wei, Z.; Li, J.; Chen, H.; Yi, Y.; Zheng, X.; Long, X.; Wang, Z.; Wang, J.; Xu, J.; et al. High-Performance Graphene-Based Hole Conductor-Free Perovskite Solar Cells: Schottky Junction Enhanced Hole Extraction and Electron Blocking. *Small* **2015**, *11*, 2269–2274. [CrossRef]
52. Heo, J.H.; Shin, D.H.; Kim, S.; Jang, M.H.; Lee, M.H.; Seo, S.W.; Choi, S.-H.; Im, S.H. Highly Efficient $CH_3NH_3PbI_3$ Perovskite Solar Cells Prepared by $AuCl_3$-Doped Graphene Transparent Conducting Electrodes. *Chem. Eng. J.* **2017**, *323*, 153–159. [CrossRef]
53. Hadadian, M.; Correa-Baena, J.-P.; Goharshadi, E.K.; Ummadisingu, A.; Seo, J.-Y.; Luo, J.; Gholipour, S.; Zakeeruddin, S.M.; Saliba, M.; Abate, A.; et al. Enhancing Efficiency of Perovskite Solar Cells via N-doped Graphene: Crystal Modification and Surface Passivation. *Adv. Mater.* **2016**, *28*, 8681–8686. [CrossRef]
54. Fang, X.; Ding, J.; Yuan, N.; Sun, P.; Lv, M.; Ding, G.; Zhu, C. Graphene Quantum Dot Incorporated Perovskite Films: Passivating Grain Boundaries and Facilitating Electron Extraction. *Phys. Chem. Chem. Phys.* **2017**, *19*, 6057–6063. [CrossRef] [PubMed]
55. Mahmoudi, T.; Wang, Y.; Hahn, Y.-B. $SrTiO_3/Al_2O_3$-Graphene Electron Transport Layer for Highly Stable and Efficient Composites-Based Perovskite Solar Cells with 20.6% Efficiency. *Adv. Energy Mater.* **2020**, *10*, 1903369. [CrossRef]
56. Xie, J.; Huang, K.; Yu, X.; Yang, Z.; Xiao, K.; Qiang, Y.; Zhu, X.; Xu, L.; Wang, P.; Cui, C.; et al. Enhanced Electronic Properties of SnO_2 via Electron Transfer from Graphene Quantum Dots for Efficient Perovskite Solar Cells. *ACS Nano* **2017**, *11*, 9176–9182. [CrossRef]
57. Luo, Q.; Zhang, Y.; Liu, C.; Li, J.; Wang, N.; Lin, H. Iodide-Reduced Graphene Oxide with Dopant-Free Spiro-OMeTAD for Ambient Stable and High-Efficiency Perovskite Solar Cells. *J. Mater. Chem. A* **2015**, *3*, 15996–16004. [CrossRef]
58. Wen, X.; Wu, J.; Gao, D.; Lin, C. Interfacial Engineering with Amino-Functionalized Graphene for Efficient Perovskite Solar Cells. *J. Mater. Chem. A* **2016**, *4*, 13482–13487. [CrossRef]
59. Yang‡, Q.-D.; Li, J.; Cheng, Y.; Li, H.-W.; Guan, Z.; Yu, B.; Tsang, S.-W. Graphene Oxide as an Efficient Hole-Transporting Material for High-Performance Perovskite Solar Cells with Enhanced Stability. *J. Mater. Chem. A* **2017**, *5*, 9852–9858. [CrossRef]
60. Zhao, X.; Tao, L.; Li, H.; Huang, W.; Sun, P.; Liu, J.; Liu, S.; Sun, Q.; Cui, Z.; Sun, L.; et al. Efficient Planar Perovskite Solar Cells with Improved Fill Factor via Interface Engineering with Graphene. *Nano Lett.* **2018**, *18*, 2442–2449. [CrossRef]
61. Agresti, A.; Pescetelli, S.; Palma, A.L.; Del Rio Castillo, A.E.; Konios, D.; Kakavelakis, G.; Razza, S.; Cinà, L.; Kymakis, E.; Bonaccorso, F.; et al. Graphene Interface Engineering for Perovskite Solar Modules: 12.6% Power Conversion Efficiency over 50 cm^2 Active Area. *ACS Energy Lett.* **2017**, *2*, 279–287. [CrossRef]
62. Hu, X.; Jiang, H.; Li, J.; Ma, J.; Yang, D.; Liu, Z.; Gao, F.; Liu, S. Air and Thermally Stable Perovskite Solar Cells with CVD-Graphene as the Blocking Layer. *Nanoscale* **2017**, *9*, 8274–8280. [CrossRef]
63. Wang, J.T.-W.; Ball, J.M.; Barea, E.M.; Abate, A.; Alexander-Webber, J.A.; Huang, J.; Saliba, M.; Mora-Sero, I.; Bisquert, J.; Snaith, H.J.; et al. Low-Temperature Processed Electron Collection Layers of Graphene/TiO_2 Nanocomposites in Thin Film Perovskite Solar Cells. *Nano Lett.* **2014**, *14*, 724–730. [CrossRef] [PubMed]
64. Yang, P.; Hu, Z.; Zhao, X.; Chen, D.; Lin, H.; Lai, X.; Yang, L. Cesium-Containing Perovskite Solar Cell Based on Graphene/TiO_2 Electron Transport Layer. *ChemistrySelect* **2017**, *2*, 9433–9437. [CrossRef]
65. Cho, K.T.; Grancini, G.; Lee, Y.; Konios, D.; Paek, S.; Kymakis, E.; Nazeeruddin, M.K. Beneficial Role of Reduced Graphene Oxide for Electron Extraction in Highly Efficient Perovskite Solar Cells. *ChemSusChem* **2016**, *9*, 3040–3044. [CrossRef] [PubMed]
66. Agresti, A.; Pescetelli, S.; Taheri, B.; Del Rio Castillo, A.E.; Cinà, L.; Bonaccorso, F.; Di Carlo, A. Graphene–Perovskite Solar Cells Exceed 18 % Efficiency: A Stability Study. *ChemSusChem* **2016**, *9*, 2609–2619. [CrossRef] [PubMed]

67. Nouri, E.; Mohammadi, M.R.; Xu, Z.-X.; Dracopoulos, V.; Lianos, P. Improvement of The Photovoltaic Parameters of Perovskite Solar Cells Using a Reduced-Graphene-Oxide-Modified Titania Layer and Soluble Copper Phthalocyanine as a Hole Transporter. *Phys. Chem. Chem. Phys.* **2018**, *20*, 2388–2395. [CrossRef] [PubMed]
68. Patil, J.V.; Mali, S.S.; Patil, A.P.; Patil, P.S.; Hong, C.K. Highly Efficient Mixed-Halide Mixed-Cation Perovskite Solar Cells Based on rGO-TiO_2 Composite Nanofibers. *Energy* **2019**, *189*, 116396. [CrossRef]
69. Xia, H.; Ma, Z.; Xiao, Z.; Zhou, W.; Zhang, H.; Du, C.; Zhuang, J.; Cheng, X.; Liu, X.; Huang, Y. Interfacial Modification Using Ultrasonic Atomized Graphene Quantum Dots for Efficient Perovskite Solar Cells. *Org. Electron.* **2019**, *75*, 105415. [CrossRef]
70. Yang, Z.; Xie, J.; Arivazhagan, V.; Xiao, K.; Qiang, Y.; Huang, K.; Hu, M.; Cui, C.; Yu, X.; Yang, D. Efficient and Highly Light Stable Planar Perovskite Solar Cells with Graphene Quantum Dots Doped PCBM Electron Transport Layer. *Nano Energy* **2017**, *40*, 345–351. [CrossRef]
71. Bi, E.; Chen, H.; Xie, F.; Wu, Y.; Chen, W.; Su, Y.; Islam, A.; Grätzel, M.; Yang, X.; Han, L. Diffusion Engineering of Ions and Charge Carriers for Stable Efficient Perovskite Solar Cells. *Nat. Commun.* **2017**, *8*, 15330. [CrossRef]
72. Kakavelakis, G.; Maksudov, T.; Konios, D.; Paradisanos, I.; Kioseoglou, G.; Stratakis, E.; Kymakis, E. Efficient and Highly Air Stable Planar Inverted Perovskite Solar Cells with Reduced Graphene Oxide Doped PCBM Electron Transporting Layer. *Adv. Energy Mater.* **2017**, *7*, 1602120. [CrossRef]
73. Shin, D.H.; Kim, J.M.; Shin, S.H.; Choi, S.-H. Highly-Flexible Graphene Transparent Conductive Electrode/Perovskite Solar Cells with Graphene Quantum Dots-Doped PCBM Electron Transport Layer. *Dye. Pigment.* **2019**, *170*, 107630. [CrossRef]
74. Chandrasekhar, P.S.; Dubey, A.; Qiao, Q. High Efficiency Perovskite Solar Cells Using Nitrogen-Doped Graphene/ZnO Nanorod Composite as an Electron Transport Layer. *Sol. Energy* **2020**, *197*, 78–83. [CrossRef]
75. Ahmed, M.I.; Hussain, Z.; Mujahid, M.; Khan, A.N.; Javaid, S.S.; Habib, A. Low Resistivity ZnO-GO Electron Transport Layer Based $CH_3NH_3PbI_3$ Solar Cells. *AIP Adv.* **2016**, *6*, 065303. [CrossRef]
76. Chandrasekhar, P.S.; Komarala, V.K. Graphene/ZnO Nanocomposite as an Electron Transport Layer for Perovskite Solar Cells; the Effect of Graphene Concentration on Photovoltaic Performance. *RSC Adv.* **2017**, *7*, 28610–28615. [CrossRef]
77. Chen, H.; Luo, Q.; Liu, T.; Tai, M.; Lin, J.; Murugadoss, V.; Lin, H.; Wang, J.; Guo, Z.; Wang, N. Boosting Multiple Interfaces by Co-Doped Graphene Quantum Dots for High Efficiency and Durability Perovskite Solar Cells. *Acs Appl. Mater. Interfaces* **2020**, *12*, 13941–13949. [CrossRef] [PubMed]
78. Kim, G.-H.; Jang, H.; Yoon, Y.J.; Jeong, J.; Park, S.Y.; Walker, B.; Jeon, I.-Y.; Jo, Y.; Yoon, H.; Kim, M.; et al. Fluorine Functionalized Graphene Nano Platelets for Highly Stable Inverted Perovskite Solar Cells. *Nano Lett.* **2017**, *17*, 6385–6390. [CrossRef] [PubMed]
79. Lamanna, E.; Matteocci, F.; Calabrò, E.; Serenelli, L.; Salza, E.; Martini, L.; Menchini, F.; Izzi, M.; Agresti, A.; Pescetelli, S.; et al. Mechanically Stacked, Two-Terminal Graphene-Based Perovskite/Silicon Tandem Solar Cell with Efficiency over 26%. *Joule* **2020**, *4*, 865–881. [CrossRef]
80. Taheri-Ledari, R.; Valadi, K.; Maleki, A. High-performance HTL-Free Perovskite Solar Cell: An Efficient Composition of ZnO NRs, RGO, and $CuInS_2$ QDs, as electron-transporting layer matrix. *Prog. Photovolt. Res. Appl.* **2020**. [CrossRef]
81. Tavakoli, M.M.; Tavakoli, R.; Nourbakhsh, Z.; Waleed, A.; Virk, U.S.; Fan, Z. High Efficiency and Stable Perovskite Solar Cell Using ZnO/rGO QDs as an Electron Transfer Layer. *Adv. Mater. Interfaces* **2016**, *3*, 1500790. [CrossRef]
82. Hanaor, D.A.H.; Sorrell, C.C. Review of the anatase to rutile phase transformation. *J. Mater. Sci.* **2011**, *46*, 855–874. [CrossRef]
83. Kim, H.-S.; Lee, J.-W.; Yantara, N.; Boix, P.P.; Kulkarni, S.A.; Mhaisalkar, S.; Grätzel, M.; Park, N.-G. High Efficiency Solid-State Sensitized Solar Cell-Based on Submicrometer Rutile TiO_2 Nanorod and $CH_3NH_3PbI_3$ Perovskite Sensitizer. *Nano Lett.* **2013**, *13*, 2412–2417. [CrossRef] [PubMed]
84. Jiang, Q.; Sheng, X.; Li, Y.; Feng, X.; Xu, T. Rutile TiO_2 Nanowire-Based Perovskite Solar Cells. *Chem. Commun.* **2014**, *50*, 14720–14723. [CrossRef] [PubMed]
85. Lee, J.-W.; Lee, T.-Y.; Yoo, P.J.; Grätzel, M.; Mhaisalkar, S.; Park, N.-G. Rutile TiO_2-Based Perovskite Solar Cells. *J. Mater. Chem. A* **2014**, *2*, 9251–9259. [CrossRef]
86. Yu, Y.; Li, J.; Geng, D.; Wang, J.; Zhang, L.; Andrew, T.L.; Arnold, M.S.; Wang, X. Development of Lead Iodide Perovskite Solar Cells Using Three-Dimensional Titanium Dioxide Nanowire Architectures. *ACS Nano* **2015**, *9*, 564–572. [CrossRef] [PubMed]

87. Mohamad Noh, M.F.; Teh, C.H.; Daik, R.; Lim, E.L.; Yap, C.C.; Ibrahim, M.A.; Ahmad Ludin, N.; Mohd Yusoff, A.R.b.; Jang, J.; Mat Teridi, M.A. The Architecture of the Electron Transport Layer for a Perovskite Solar Cell. *J. Mater. Chem. C* **2018**, *6*, 682–712. [CrossRef]
88. Kim, H.-S.; Park, N.-G. Parameters Affecting I–V Hysteresis of $CH_3NH_3PbI_3$ Perovskite Solar Cells: Effects of Perovskite Crystal Size and Mesoporous TiO_2 Layer. *J. Phys. Chem. Lett.* **2014**, *5*, 2927–2934. [CrossRef] [PubMed]
89. Jeon, N.J.; Noh, J.H.; Kim, Y.C.; Yang, W.S.; Ryu, S.; Seok, S.I. Solvent Engineering for High-Performance Inorganic–Organic Hybrid Perovskite Solar Cells. *Nat. Mater.* **2014**, *13*, 897–903. [CrossRef]
90. Tiwana, P.; Docampo, P.; Johnston, M.B.; Snaith, H.J.; Herz, L.M. Electron Mobility and Injection Dynamics in Mesoporous ZnO, SnO_2, and TiO_2 Films Used in Dye-Sensitized Solar Cells. *ACS Nano* **2011**, *5*, 5158–5166. [CrossRef]
91. Leijtens, T.; Eperon, G.E.; Pathak, S.; Abate, A.; Lee, M.M.; Snaith, H.J. Overcoming Ultraviolet Light Instability of Sensitized TiO_2 with Meso-superstructured Organometal Tri-halide Perovskite Solar Cells. *Nat. Commun.* **2013**, *4*, 2885. [CrossRef]
92. Liu, D.; Wang, Y.; Xu, H.; Zheng, H.; Zhang, T.; Zhang, P.; Wang, F.; Wu, J.; Wang, Z.; Chen, Z.; et al. SnO_2-Based Perovskite Solar Cells: Configuration Design and Performance Improvement. *Sol. RRL* **2019**, *3*, 1800292. [CrossRef]
93. Ke, W.; Fang, G.; Liu, Q.; Xiong, L.; Qin, P.; Tao, H.; Wang, J.; Lei, H.; Li, B.; Wan, J.; et al. Low-Temperature Solution-Processed Tin Oxide as an Alternative Electron Transporting Layer for Efficient Perovskite Solar Cells. *J. Am. Chem. Soc.* **2015**, *137*, 6730–6733. [CrossRef] [PubMed]
94. Jarzebski, Z.M.; Morton, J.P. Physical Properties of SnO_2 Materials: III. Optical Properties. *J. Electrochem. Soc.* **2019**, *123*, 333C–346C. [CrossRef]
95. Jarzebski, Z.M.; Marton, J.P. Physical Properties of SnO_2 Materials: II. Semiconducting properties. *J. Electrochem. Soc.* **2019**, *123*, 299C–310C. [CrossRef]
96. Yang, D.; Yang, R.; Wang, K.; Wu, C.; Zhu, X.; Feng, J.; Ren, X.; Fang, G.; Priya, S.; Liu, S. High Efficiency Planar-Type Perovskite Solar Cells with Negligible Hysteresis Using EDTA-Complexed SnO_2. *Nat. Commun.* **2018**, *9*, 3239. [CrossRef] [PubMed]
97. Jiang, Q.; Chu, Z.; Wang, P.; Yang, X.; Liu, H.; Wang, Y.; Yin, Z.; Wu, J.; Zhang, X.; You, J. Planar-Structure Perovskite Solar Cells with Efficiency beyond 21%. *Adv. Mater.* **2017**, *29*, 1703852. [CrossRef] [PubMed]
98. Barbé, J.; Tietze, M.L.; Neophytou, M.; Murali, B.; Alarousu, E.; Labban, A.E.; Abulikemu, M.; Yue, W.; Mohammed, O.F.; McCulloch, I.; et al. Amorphous Tin Oxide as a Low-Temperature-Processed Electron-Transport Layer for Organic and Hybrid Perovskite Solar Cells. *ACS Appl. Mater. Interfaces* **2017**, *9*, 11828–11836. [CrossRef]
99. Anaraki, E.H.; Kermanpur, A.; Steier, L.; Domanski, K.; Matsui, T.; Tress, W.; Saliba, M.; Abate, A.; Grätzel, M.; Hagfeldt, A.; et al. Highly Efficient and Stable Planar Perovskite Solar Cells by Solution-Processed Tin Oxide. *Energy Environ. Sci.* **2016**, *9*, 3128–3134. [CrossRef]
100. Roose, B.; Baena, J.-P.C.; Gödel, K.C.; Graetzel, M.; Hagfeldt, A.; Steiner, U.; Abate, A. Mesoporous SnO_2 Electron Selective Contact Enables UV-Stable Perovskite Solar Cells. *Nano Energy* **2016**, *30*, 517–522. [CrossRef]
101. Deng, K.; Chen, Q.; Li, L. Modification Engineering in SnO_2 Electron Transport Layer toward Perovskite Solar Cells: Efficiency and Stability. *Adv. Funct. Mater.* **2020**, *30*, 2004209. [CrossRef]
102. Özgür, Ü.; Alivov, Y.I.; Liu, C.; Teke, A.; Reshchikov, M.A.; Doğan, S.; Avrutin, V.; Cho, S.J.; Morkoç, H. A Comprehensive Review of ZnO Materials and Devices. *J. Appl. Phys.* **2005**, *98*, 041301. [CrossRef]
103. Haase, M.; Weller, H.; Henglein, A. Photochemistry and Radiation Chemistry of Colloidal Semiconductors. 23. Electron Storage on Zinc Oxide Particles and Size Quantization. *J. Phys. Chem.* **1988**, *92*, 482–487. [CrossRef]
104. Liu, D.; Kelly, T.L. Perovskite Solar Cells with a Planar Heterojunction Structure Prepared Using Room-Temperature Solution Processing Techniques. *Nat. Photonics* **2014**, *8*, 133–138. [CrossRef]
105. Yang, J.; Siempelkamp, B.D.; Mosconi, E.; De Angelis, F.; Kelly, T.L. Origin of the Thermal Instability in $CH_3NH_3PbI_3$ Thin Films Deposited on ZnO. *Chem. Mater.* **2015**, *27*, 4229–4236. [CrossRef]
106. Said, A.A.; Xie, J.; Zhang, Q. Recent Progress in Organic Electron Transport Materials in Inverted Perovskite Solar Cells. *Small* **2019**, *15*, 1900854. [CrossRef] [PubMed]
107. Shao, Y.; Xiao, Z.; Bi, C.; Yuan, Y.; Huang, J. Origin and Elimination of Photocurrent Hysteresis by Fullerene Passivation in $CH_3NH_3PbI_3$ Planar Heterojunction Solar Cells. *Nat. Commun.* **2014**, *5*, 5784. [CrossRef] [PubMed]

108. Xu, J.; Buin, A.; Ip, A.H.; Li, W.; Voznyy, O.; Comin, R.; Yuan, M.; Jeon, S.; Ning, Z.; McDowell, J.J.; et al. Perovskite–Fullerene Hybrid Materials Suppress Hysteresis in Planar Diodes. *Nat. Commun.* **2015**, *6*, 7081. [CrossRef]
109. Tavakoli, M.M.; Tavakoli, R.; Hasanzadeh, S.; Mirfasih, M.H. Interface Engineering of Perovskite Solar Cell Using a Reduced-Graphene Scaffold. *J. Phys. Chem. C* **2016**, *120*, 19531–19536. [CrossRef]